

1 **Do olivine crystallization temperatures faithfully record**
2 **mantle temperature variability?**

3 **Simon Matthews^{1*}, Kevin Wong^{1,2}, Oliver Shorttle^{1,3}, Marie Edmonds¹, John**
4 **MacLennan¹**

5 ¹Department of Earth Sciences, University of Cambridge, Cambridge, U.K., CB2 3EQ

6 ²School of Earth and Environment, University of Leeds, Leeds, U.K., LS2 9JT

7 ³Institute of Astronomy, University of Cambridge, Cambridge, U.K., CB3 0HA

8 **Manuscript accepted for publication in G3 on 1st February 2021.**

9 **Key Points:**

- 10 • Hawaiian olivines crystallize at hotter temperatures than olivines in MORB
11 • Models are developed to link crystallization temperature to mantle temperature
12 • Mantle plumes may have had a similar distribution of temperatures throughout the
13 Phanerozoic

*Now at Institute of Earth Sciences, University of Iceland, Sturlugata 7, 102 Reykjavík, Iceland.

Corresponding author: Simon Matthews, simonm@hi.is

Abstract

Crystallization temperatures of primitive olivine crystals have been widely used as both a proxy for, or an intermediate step in calculating, mantle temperatures. The olivine-spinel aluminum-exchange thermometer has been applied to samples from mid-ocean ridges and large igneous provinces, yielding considerable variability in olivine crystallization temperatures. We supplement the existing data with new crystallization temperature estimates for Hawaii, between 1282 ± 21 and $1375 \pm 19^\circ\text{C}$.

Magmatic temperatures may be linked to mantle temperatures if the thermal changes during melting can be quantified. The magnitude of this temperature change depends on melt fraction, itself controlled by mantle temperature, mantle composition and lithosphere thickness. Both mantle composition and lithosphere thickness vary spatially and temporally, with systematic differences between mid-ocean ridges, ocean islands and large igneous provinces. For crystallization temperatures to provide robust evidence of mantle temperature variability, the controls of lithosphere thickness and mantle lithology on crystallization temperature must be isolated.

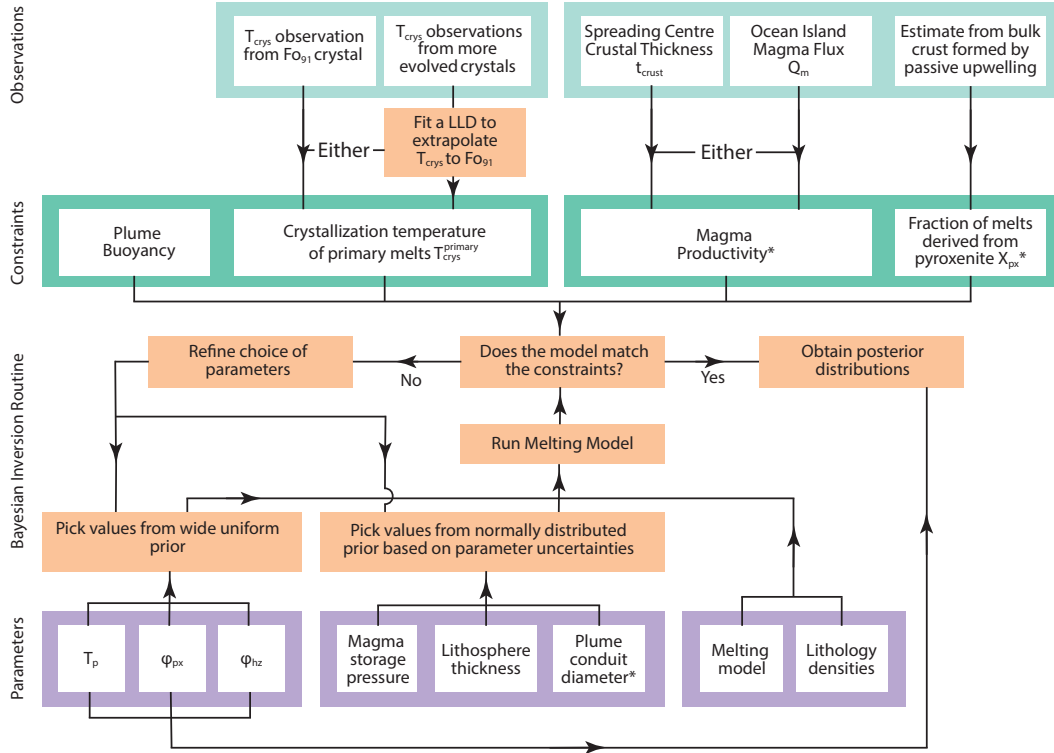
We develop a multi-lithology melting model for predicting crystallization temperatures of magmas in both intra-plate volcanic provinces and mid-ocean ridges. We find that the high crystallization temperatures seen at mantle plume localities do require high mantle temperatures. In the absence of further constraints on mantle lithology or melt productivity, we cannot robustly infer variable plume temperatures between ocean-islands and large igneous provinces from crystallization temperatures alone; for example, the extremely high crystallization temperatures obtained for the Tortugal Phanerozoic komatiite could derive from mantle of comparable temperature to modern-day Hawaii. This work demonstrates the limit of petrological thermometers when other geodynamic parameters are poorly known.

1 Introduction

Temperature variations in Earth's mantle drive its vigorous convective circulation, which governs the thermal and chemical exchanges between Earth's interior and exterior reservoirs. When convective upwellings, or plumes, first impact the Earth's lithospheric shell, voluminous magma generation creates large igneous provinces (LIPs) (e.g., Campbell & Griffiths, 1990; White & McKenzie, 1989). Many regions of modern-day intra-plate magmatism have also been linked to melting in plumes, with the plume's magma productivity diminishing over time (e.g., Wilson, 1973; Richards et al., 1989).

Mapping the spatial and temporal variability in mantle plume temperatures is key for constraining dynamical models of mantle convection (e.g., Campbell et al., 1989; Griffiths & Campbell, 1990; Farnetani & Richards, 1995; Dannberg & Sobolev, 2015) and for understanding the evolution of magmatism throughout Earth history (e.g., Herzberg & Gazel, 2009; Putirka, 2016). A variety of geochemical and geophysical observations have been interpreted as indicating that modern-day mantle plume temperatures vary substantially (e.g., Putirka, 2008a; Herzberg & Asimow, 2015) and that individual plume temperatures may have changed through time (e.g., White, 1993; Parnell-Turner et al., 2014), particularly in the transition from large igneous province to ocean island volcanism (e.g., Thompson & Gibson, 2000; Hole & Millett, 2016; Spice et al., 2016).

A significant challenge in estimating mantle temperature variability is raised by variations in the tectonic regime of volcanism; mantle dynamics, the melting process, and mantle composition are likely to vary systematically with tectonic regime. Accounting adequately for these parameters when calculating mantle temperatures is particularly important when comparing the mantle sampled by mid-ocean ridge basalt (MORB), ocean-island basalt (OIB), and LIP magmatism. It also presents a challenge when extending methods of mantle temperature estimation into deep time, where these geodynamic parameters are more poorly constrained.



78 **Figure 1.** Summary of our approach to estimating mantle potential temperature, T_p , pyroxenite fraction, ϕ_{px} , harzburgite fraction, ϕ_{hz} , from raw observations of T_{cryst} and magmatic flux.
 79 *Parameters not used in every inversion.
 80

64 In this study we consider how well variations in crystallization temperature of primitive
 65 olivine crystals can constrain the spatial and temporal variability in mantle plume
 66 temperatures. To this end we use crystallization temperatures obtained from the olivine-
 67 spinel aluminum-exchange thermometer (Coogan et al., 2014, Section 2). As a reference
 68 for modern-day OIB magmatism, we present new olivine crystallization temperatures for
 69 Hawaii (Section 3). In Section 4 we develop a toolkit for extracting the temperature at
 70 which magmas most likely began to crystallize, when olivine populations have highly vari-
 71 able crystallization temperature. By extending the mantle melting models developed by
 72 Matthews et al. (2016) and Shorttle et al. (2014) we quantify the relationship between
 73 crystallization temperature and mantle temperature, subject to variable tectonic setting
 74 and mantle composition (Section 5). Finally we invert our melting model (Section 6) to
 75 quantify mantle temperatures, using both our new crystallization temperature dataset, and
 76 similar datasets for global MORB, OIB and LIP localities (Section 7). Our approach is
 77 summarised in Figure 1.

81 1.1 The ubiquity of harzburgite in the mantle

82 Harzburgitic residues are the inevitable products of extensive melt extraction from the
 83 mantle. It might be expected that mantle harzburgites have been generated throughout
 84 Earth’s history, initially making up lithospheric mantle, but ultimately being convectively
 85 stirred back into the mantle (e.g., Langmuir et al., 1992). Harzburgite units are observed at
 86 the base of ophiolites, thought to represent the residue of melting beneath the ridge crest
 87 (e.g., Boudier & Coleman, 1981; Godard et al., 2000), confirming that harzburgitic rocks are
 88 produced, at least at some spreading centres. Their very origin as melting residues means

89 that they are both extremely refractory and highly depleted in trace elements. In some
 90 melting regions harzburgitic mantle components may not melt at all, and even if they do,
 91 the trace element budget of erupted basalts will be overwhelmed by less depleted mantle
 92 components, and any isotopic record of extreme depletion will be rapidly mixed out (Rudge
 93 et al., 2013; Byerly & Lassiter, 2014). Nevertheless, isotope ratio evidence for the presence
 94 of ancient and extremely depleted mantle components has been found in both MORB lavas
 95 (Salters et al., 2011) and OIB melt inclusions (Stracke et al., 2019)

96 Whilst we might expect radiogenic isotope signatures of extreme melt depletion to go
 97 hand-in-hand with lithological evolution to harzburgite, isotope ratios do not directly con-
 98 strain source lithology. More direct evidence for the ubiquity of harzburgite in the convecting
 99 mantle comes from mantle peridotites now exposed at Earth’s surface. Harzburgitic abyssal
 100 peridotites are seen in a number of spreading segments which have only small amounts of
 101 melt generation (Seyler et al., 2004; Paulick et al., 2006; Lassiter et al., 2014; D’Errico
 102 et al., 2016). The absence of substantial melt generation suggests that these harzburgites
 103 were generated in an ancient melting event and have been recycled through the convecting
 104 mantle. This is supported by extremely depleted radiogenic isotope ratios in these abyssal
 105 peridotites (Harvey et al., 2006; Liu et al., 2008; Warren et al., 2009; Stracke et al., 2011;
 106 Warren & Shirey, 2012; Mallick et al., 2015), in addition to some ocean-island harzburgite
 107 xenoliths (Salters & Zindler, 1995; Bizimis et al., 2007), which together were described as
 108 unequivocal evidence for ancient melt-extraction by Warren (2016).

109 Further indirect constraints on harzburgite abundances come from modelling by Shorttle
 110 et al. (2014) and Matthews et al. (2016), who incorporated a non-melting harzburgite com-
 111 ponent into their melting models. Shorttle et al. (2014) calculated plume buoyancy as a
 112 function of mantle temperature, pyroxenite fraction, and harzburgite fraction, and demon-
 113 strated that a significant quantity of harzburgite is required in the Iceland and Hawaiian
 114 plumes to satisfy plume volume flux constraints. Matthews et al. (2016) further constrained
 115 a harzburgite fraction of $47^{+16}_{-19}\%$ in the Icelandic plume in order to simultaneously recreate
 116 the trace element concentrations, crustal thickness, and crystallization temperatures in Ice-
 117 land’s Northern Volcanic Zone. The same process suggested a similar harzburgite fraction
 118 in the mantle beneath the Siqueiros fracture zone on the East Pacific Rise.

119 It is, therefore, very unlikely that there is not at least some harzburgite present in
 120 the mantle whence MORB and OIB derive. Whilst the harzburgite component might not
 121 contribute much, or any, magma, it will have an effect on the geothermal gradient in the
 122 melting region in its capacity as a thermal buffer (Phipps Morgan, 2001; Shorttle et al., 2014;
 123 Matthews et al., 2016). This influence on the thermal structure of the melting region will
 124 affect the temperatures at which magmas leave the mantle and ultimately begin crystallising
 125 (Matthews et al., 2016) and could change both their major- and trace-element compositions
 126 (Appendix A). For these reasons, the models we present here allow, but do not require,
 127 significant mantle harzburgite fractions. The uncertainty in harzburgite prevalence has a
 128 large contribution to the propagated uncertainty on our estimates of T_p , and is one among
 129 many reasons why diverse primary crystallization temperatures could be consistent with
 130 similar mantle T_p .

131 We emphasise that when we discuss mantle harzburgite we are considering harzburgitic
 132 lithologies present before the onset of the melting event we are tracing. Additionally, in some
 133 locations, melting of the lherzolite and pyroxenite lithologies is predicted to continue until
 134 clinopyroxene-exhaustion, which will leave behind a harzburgitic residue. This behaviour is
 135 explicitly included within the lherzolite and pyroxenite melting models.

136 *1.1.1 The effects of harzburgite and pyroxenite on mantle melt fractions*

137 When a considerable quantity of refractory (harzburgite) or anomalously fusible (py-
 138 roxenite) material is present in the mantle it affects both the bulk melt fraction and the
 139 melt fractions of the other lithologies present (Shorttle et al., 2014; Matthews et al., 2016).

140 Substantially lower quantities, or even zero, melt may be generated from a harzburgitic
 141 component during upwelling. This decreases the bulk melt fraction, and consequently the
 142 crustal thickness at spreading ridges, or magmatic flux more generally. However, since there
 143 is no latent heat being extracted by harzburgite melting, more heat energy is available to the
 144 other lithologies, assuming they remain in thermal equilibrium with each other. Any lherz-
 145 zolite or pyroxenite present may, therefore, achieve higher melt fractions than they would
 146 in a harzburgite-free mantle of the same temperature.

147 Conversely, when a substantial quantity of anomalously fusible material is present, the
 148 large extent of melting will extract more latent heat, decreasing the heat energy available
 149 to the other lithologies. The presence of pyroxenite may thus have the opposite effect of
 150 harzburgite on the other lithologies: lower melt fractions will be obtained than at the same
 151 temperature, though the bulk melt fraction may be higher owing to the large contribution
 152 from fusible pyroxenite.

153 The composition of lherzolite- and pyroxenite-derived melts is determined by the pres-
 154 sure and temperature (or melt-fraction) at which they were formed. In Section 1.2.1 we
 155 briefly review approaches utilising magma composition to estimate mantle temperatures,
 156 the first step of which is to estimate the mantle melt fraction. Necessarily, a melt fraction
 157 estimated in this manner applies only to a single lithology, generally lherzolite. If there is
 158 a significant harzburgite fraction or pyroxenite fraction, the bulk melt fraction of the man-
 159 tle may be significantly lower or higher than the lherzolite melt fraction. It is important,
 160 therefore, to distinguish bulk mantle melt fraction from the melt fractions of individual
 161 lithologies.

162 **1.2 Estimating mantle temperatures**

163 An assortment of petrological and geophysical techniques have been employed in es-
 164 timating mantle temperature variability. Whilst geophysical observations can provide con-
 165 straints on modern-day mantle temperatures (e.g., Watson & M^cKenzie, 1991; Jenkins et
 166 al., 2016), our focus is on using petrological observations. Petrological observations can be
 167 made not only on recently erupted basalts, representing the present-day thermal state of
 168 plumes, but also on ancient volcanics associated with LIPs. Petrological techniques take
 169 advantage of the controls exerted by temperature and pressure on mineral stability and
 170 magma composition, to constrain temperatures within magmatic systems. A model for the
 171 thermal changes accompanying mantle decompression and melting must then be applied to
 172 estimate the temperature of solid mantle beneath the melting region. To normalise out the
 173 effect of decompression on mantle temperature, we use the mantle potential temperature,
 174 T_p : the temperature mantle material would have were it to be transported to the surface
 175 without chemical change (Cawthorn, 1975; M^cKenzie & Bickle, 1988).

176 **1.2.1 Estimating T_p from magma chemistry**

177 The composition of primary mantle melts betrays the temperatures and pressures at
 178 which they formed, and the mantle lithology whence they derived. Experimental work (e.g.,
 179 Kinzler & Grove, 1992) has constrained the relationship between melting conditions and
 180 primary melt chemistry, enabling the development of empirical expressions to quantify that
 181 relationship (e.g., M^cKenzie & Bickle, 1988; Lee et al., 2009). However, erupted lavas are not
 182 primary mantle melts, having undergone fractional crystallization and mixing, progressively
 183 modifying their chemistry (e.g., O'Hara, 1965; O'Hara, 1968; Klein & Langmuir, 1987;
 184 Grove et al., 1992; MacLennan, 2008; Rudge et al., 2013; Hole & Natland, 2019). The
 185 presence of pyroxenite in the mantle source of melts creates additional complexity; at any
 186 given pressure and temperature, the chemistry of melts in equilibrium with pyroxenite is
 187 different from melts in equilibrium with mantle lherzolite (e.g., Hirschmann & Stolper, 1996;
 188 Lambart et al., 2013; Jennings et al., 2016). The chemistry of a mixed magma, containing
 189 substantial contributions from both lherzolite and pyroxenite, is difficult to use to directly

190 estimate melting temperature and pressure. Fortunately, volcanic provinces often have lavas
 191 with minimal contribution from pyroxenite melts, even where pyroxenite is present in the
 192 mantle source (e.g., Herzberg & Asimow, 2008; Shorttle & MacLennan, 2011).

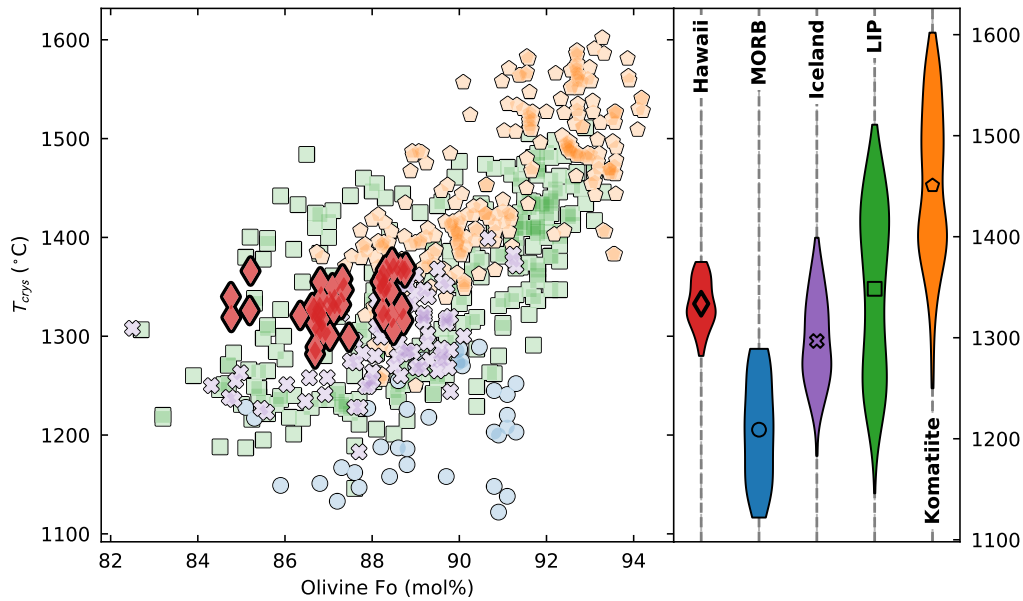
193 For the chemistry of natural lavas to be of use in obtaining the temperature and
 194 pressure of magma genesis, the composition of their ancestral primary mantle melt must
 195 be estimated by undoing the chemical changes caused by fractional crystallization. The
 196 PRIMELT3 program (Herzberg & Asimow, 2015) implements an algorithm that adds olivine
 197 back into an olivine-saturated lava until its composition resembles a primary melt of the
 198 KR4003 lherzolite (Walter, 1998). When lithologically homogeneous mantle melts by adi-
 199 abatic decompression, the melt MgO content remains approximately constant throughout
 200 melting (Herzberg & O'Hara, 2002), providing a simple relationship between primary melt
 201 MgO and mantle T_p , which is utilized by PRIMELT3. Furthermore, the reconstructed
 202 magma composition constrains the melt fraction, which may be combined with the T_p esti-
 203 mate to obtain the minimum pressure of melting. However, the presence of substantial
 204 fractions of refractory harzburgite or fusible pyroxenite will change the temperature gradient
 205 in the melting region, complicating the simple relationship between primary magma MgO
 206 and mantle T_p (Appendix A).

207 Trace element concentrations in lavas have also been inverted to estimate mantle T_p
 208 (McKenzie & O'Nions, 1991). The concentrations of rare earth elements (REEs) in mantle
 209 melts, relative to the concentration in their source, are straightforward to predict, given
 210 the melt fraction and pressure. If mantle REE concentrations are known, melt fraction
 211 vs depth curves can be constructed by iterative fitting of lava REE chemistry. The melt
 212 fraction curves are then compared to the expected evolution of melt fraction with depth for
 213 different values of mantle T_p . However, plume-driven (active) upwelling (MacLennan et al.,
 214 2001), lithological heterogeneity (Appendix A), and trace element heterogeneity (Brown et
 215 al., 2020a) can complicate the application of REE-inversions.

216 **1.2.2 Estimating T_p from crystallization temperatures**

217 Rather than estimating T_p directly from lava chemistry, Putirka et al. (2007) developed
 218 a method where primary olivine crystallization temperatures are estimated first, followed by
 219 a correction for the latent heat of melting. Both steps utilize lava chemistry. The primary
 220 mantle melt X_{Mg} and X_{Fe} are reconstructed by back-projecting the olivine-controlled liquid
 221 line of descent, inferred from the lava chemistry, to find a magma that is in Mg-Fe equilibrium
 222 with the most forsteritic olivine thought to crystallize from the melt. The olivine-liquid Mg-
 223 Fe exchange thermometer (Putirka, 2005; Putirka et al., 2007) is then used to obtain a
 224 crystallization temperature. The other major-element oxide concentrations in the primary
 225 melt are then reconstructed by adding olivine to a lava composition until the X_{Mg} and
 226 X_{Fe} inferred in the previous step are obtained, analogous to the PRIMELT3 algorithm.
 227 Using the reconstructed melt composition the melt fraction is estimated, from which the
 228 latent heat of melting and the associated temperature drop are calculated. Combining the
 229 calculated temperature-drop due to melting, with the crystallization temperature, yields an
 230 estimate of the mantle T_p .

231 This method is simple to apply, but a major uncertainty arises from making the as-
 232 sumption that a particular lava sample (or its ancestral melts) was ever in equilibrium with
 233 the chosen olivine composition. Indeed, the lava samples used as the starting point for the
 234 calculation represent mixed melts. It is likely that only the most extreme unmixed melts
 235 were in equilibrium with the most forsteritic olivines, potentially leading to overestimation
 236 of primary crystallization temperatures (Herzberg, 2011; Matthews et al., 2016). Further-
 237 more, with particular relevance to Hawaii, Wieser et al. (2019) demonstrated that the most
 238 forsteritic olivine crystals from Kilauea are not cogenetic with their carrier melts, even prior
 239 to mixing.



261 **Figure 2.** New Hawaiian olivine crystallization temperature estimates, shown alongside a global
 262 compilation of olivine-spinel aluminum-exchange crystallization temperatures. The left-hand side
 263 of the figure shows the individual olivine crystallization temperatures plotted versus olivine core
 264 composition (where $Fo > 82$), and the right-hand side shows crystallization temperature kernel den-
 265 sity estimates. The compilation is subdivided into mid-ocean ridge basalt (MORB) (this study and
 266 Coogan et al., 2014), Iceland (Matthews et al., 2016; Spice et al., 2016), large igneous provinces
 267 (LIP) (Coogan et al., 2014; Heinonen et al., 2015; Jennings et al., 2019; Spice et al., 2016; Trela
 268 et al., 2017; R. Xu & Liu, 2016), and komatiites (A. V. Sobolev et al., 2016; Trela et al., 2015;
 269 Waterton et al., 2017).

240 The olivine-spinel aluminum-exchange thermometer (Wan et al., 2008; Coogan et al.,
 241 2014) can be used to estimate primitive olivine crystallization temperatures and, in contrast
 242 to the approaches described above, reconstruction of a primary magma composition is not
 243 required. Instead, co-existing olivine and spinel crystals that were in equilibrium at the
 244 time of crystallization must be identified. For olivine-spinel equilibrium to record primary
 245 crystallization temperatures, the phases must have saturated at a similar time, and these
 246 early formed crystals must have been erupted. The common occurrence of spinel inclusions
 247 in primitive olivine hosts indicates that spinel and olivine co-saturate early in many loca-
 248 tions (e.g., Coogan et al., 2014; Spice et al., 2016; Matthews et al., 2016; Trela et al., 2017),
 249 and the close spatial relationship suggests the phases were in equilibrium with the same
 250 melt (and, therefore, each other). However, in other locations (including Hawaii), spinel
 251 inclusions are only seen in more evolved olivines, and experimental work (Eggins, 1992;
 252 Wagner & Grove, 1998; Maaløe, 2004) indicates olivine and spinel co-saturation occurs at
 253 temperatures far below the liquidus. In Section 4 we consider how best to compare crys-
 254 tallization temperatures between locations where olivine and spinel co-saturate at different
 255 times. Whilst Al hosted in olivine octahedral sites via a vacancy-coupled substitution may
 256 diffuse extremely rapidly (Zhukova et al., 2017), the majority of the Al incorporated into
 257 olivine is likely to be extremely slow diffusing (Spandler & O'Neill, 2010), making it unlikely
 258 that the thermometer will be reset following crystallization (Coogan et al., 2014). Appli-
 259 cation of the thermometer has yielded systematic differences in crystallization temperature
 260 between MORB, Iceland, LIPs and komatiites (Figure 2).

270 Since we can assess the reliability of the olivine-spinel aluminum-exchange temper-
 271 atures using the petrological context of the crystals, and the temperature estimates are
 272 independent of assumptions about melt chemistry or mantle composition, we use this tech-
 273 nique in preference to the others summarized above. However, some of the datasets in
 274 the global compilation do not contain the most primitive olivines likely to have formed.
 275 Comparisons to such datasets must, therefore, be done with careful consideration of the
 276 missing crystallization history (Section 4). Once the crystallization temperatures of the
 277 most primitive olivines have been estimated, either directly from the thermometer or by
 278 extrapolating the missing crystallization history, the temperature reduction due to melting
 279 must be estimated (the latent heat of melting correction). Only then can the mantle T_p be
 280 calculated.

281 The magnitude of the latent heat of melting correction is directly related to the total
 282 melt fraction. The approaches developed by M^cKenzie and O’Nions (1991), Putirka et al.
 283 (2007), and Herzberg and Gazel (2009), reviewed above, all estimate the total melt fraction
 284 from lava composition. However, the melt fraction estimated with these approaches pertains
 285 only to the lherzolite mantle component, which may bear little resemblance to the total melt
 286 fraction when there are significant mantle pyroxenite and harzburgite fractions (Appendix
 287 A). The total melt fraction can also be constrained using observations of magmatic produc-
 288 tivity (M^cKenzie & Bickle, 1988; Shorttle et al., 2014) and by estimating the geothermal
 289 gradient through the melting region (Matthews et al., 2016; Jennings et al., 2019).

290 At all but the slowest spreading mid-ocean ridges the crustal thickness is a direct
 291 constraint on the melt fraction, and is independent of spreading rate and ridge geometry
 292 (e.g., Reid & Jackson, 1981; Bown & White, 1994). Where decompression melting results
 293 from plume-driven (active) mantle upwelling, such as at many ocean islands, the total
 294 melt fraction may be estimated from the magma flux, though the upwelling velocity and
 295 geometry of the plume must be assumed (e.g., Watson & M^cKenzie, 1991; Shorttle et al.,
 296 2014). Where available, we use either the crustal thickness at spreading centres, or the
 297 magma flux at ocean islands, to constrain our T_p inversions.

298 In the absence of a tight constraint on the melt fraction, the range of plausible latent
 299 heat of melting corrections might be considered. This can be achieved by forward modelling
 300 the geotherm throughout the melting region to find the range of solutions able to match ob-
 301 served crystallization temperatures. Once melts leave the melting region they must traverse
 302 the lithosphere until they stall in a crustal magma chamber. During transit the melts are
 303 likely to thermally equilibrate with the surrounding lithosphere, their temperatures tend-
 304 ing towards the geotherm. However, calculating the geothermal gradient in the lithosphere
 305 is more complex, being controlled both by the advection by magmas and the conduction
 306 of heat through the Earth’s surface. We make the assumption that advection of heat by
 307 magma movement dominates over conductive heat loss. In this scenario the geotherm will
 308 not deviate far from the liquid adiabat, any difference being small compared to the other
 309 uncertainties.

310 Jennings et al. (2019) employed the forward modelling approach when converting their
 311 crystallization temperatures for the Etendeka LIP into a mantle T_p . They model melting
 312 assuming a homogeneous mantle composition of KLB-1 lherzolite, and that the melts follow
 313 a liquid adiabat whilst traversing the lithosphere. In estimating T_p for MORB and Iceland,
 314 Matthews et al. (2016) also forward modelled geotherms, but allowed for variable proportions
 315 of harzburgite and pyroxenite in the mantle, constraining their T_p solutions further with
 316 observations of melt production rates (constrained by crustal thicknesses). We take this
 317 approach here, using a forward model of multi-lithologic melting to estimate the geotherm
 318 (Section 5), constrained with rates of melt production where estimates can be made (Section
 319 6).

320 Whilst geophysical techniques are used to estimate present-day lithospheric thickness
 321 (e.g., Priestley & M^cKenzie, 2006; Geissler et al., 2010), we must rely on the rock record for

322 ancient magmatic provinces. The major and trace element chemistry of lavas not only con-
 323 strains mantle T_p , but is also sensitive to the minimum pressure of melting. Both PRIMELT3
 324 (Herzberg & Asimow, 2015) and REE inversions (McKenzie & O’Nions, 1991) have been
 325 used to predict the minimum melting pressure. Whilst the estimates of lithospheric thick-
 326 ness derived from these techniques have the same limitations as their T_p estimates, they
 327 provide one of the few constraints on the lithospheric thickness contemporaneous with past
 328 melting events.

329 2 Materials and analytical methods

330 Olivine crystals were extracted from crushed tephra collected from the first episode of
 331 the Kīlauea Iki 1959 eruption, Hawaii (Sides et al., 2014a), and from the Siqueiros fracture
 332 zone whole rock sample 2384-1 (Perfit et al., 1996). Only crystals containing spinel inclusions
 333 fully enclosed by olivine were selected, avoiding spinels that are likely to have re-equilibrated
 334 with the surrounding magma following entrapment. The crystals were mounted in epoxy
 335 resin, then ground and polished with silicon carbide papers and diamond suspensions. The
 336 Loihi olivine crystals were previously prepared and analysed for melt inclusion chemistry by
 337 Sides et al. (2014a).

338 The Coogan et al. (2014) olivine-spinel aluminum-exchange thermometer requires the
 339 Al_2O_3 content of co-existing olivine and spinel, and the Cr# of the spinel:

$$T_{\text{crys}}(K) = \frac{10,000}{0.575 + 0.884\text{Cr}\# - 0.897\ln(k_d)} \quad (1)$$

340 where,

$$k_d = \frac{\text{Al}_2\text{O}_3^{\text{olivine}}}{\text{Al}_2\text{O}_3^{\text{spinel}}} \quad (2)$$

341 and,

$$\text{Cr}\# = \frac{\text{Cr}}{\text{Cr} + \text{Al}}. \quad (3)$$

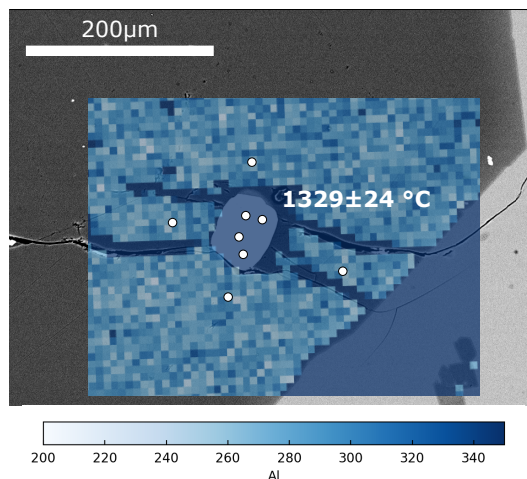
342 In these equations Al_2O_3 concentrations are in wt%, and Al and Cr are molar quantities.
 343 All chemical data were obtained using electron probe micro-analysis (Section 2.1). Error
 344 propagation was performed using a Monte Carlo method as described by Matthews et al.
 345 (2016) using a standard deviation of 14°C as the combined uncertainty on the thermometer
 346 calibration. This estimate of the uncertainty represents a minimum bound on the uncer-
 347 tainty as it is derived from the same data used to calibrate the thermometer by Coogan et
 348 al. (2014).

349 2.1 Electron probe micro-analysis

350 Analyses were performed using the Cameca SX-100 Electron Microprobe at the De-
 351 partment of Earth Sciences, University of Cambridge, over two sessions. The first session
 352 was dedicated to obtaining qualitative maps of the Al_2O_3 distribution in olivine crystals
 353 containing spinel inclusions (Section 2.1.1). These maps were used to guide the selection of
 354 points for quantitative analysis in the second session (Section 2.1.2), enabling us to char-
 355 acterize and avoid Al_2O_3 zoning, as observed in some crystals by Coogan et al. (2014) and
 356 Matthews et al. (2016).

357 2.1.1 Qualitative element mapping

358 Preliminary qualitative mapping of olivine Al and P concentrations adjacent to spinel
 359 inclusions was performed using a 15 kV 200 nA beam with a dwell time of 0.5 s per $\sim 7 \mu\text{m}$
 360 pixel. All maps were acquired by moving the stage beneath a static beam, and counts were
 361 recorded for the Al $K\alpha$ peak using the LTAP crystal, and for the P $K\alpha$ peak using the LPET
 362 crystal. Applying the same technique to a crystal where Al-zoning was previously observed



371 **Figure 3.** Back-scatter electron image superimposed with the qualitative Al map for olivine-
 372 spinel pair L.F4. The color scale shows the counts on the Al $K\alpha$ peak. White dots show the location
 373 of quantitative analyses. The temperature calculated for this olivine-spinel pair is shown.

363 by Matthews et al. (2016) demonstrated these conditions were appropriate for identifying
 364 zoning (Supporting Figure S.1.). The maps are provided in Supporting Data Set S.4.

365 Using the maps of Al and P concentrations, we selected points for quantitative analysis,
 366 preferring regions of homogeneous Al concentration and low P concentration adjacent to
 367 the spinel inclusion (Figure 3). Regions of high P concentration are best avoided since its
 368 incorporation into olivine correlates with increased uptake of Al (Coogan et al., 2014). The
 369 majority of crystals did not show any variability in Al concentration on the scale of the
 370 map, and P concentrations were below the detection limit.

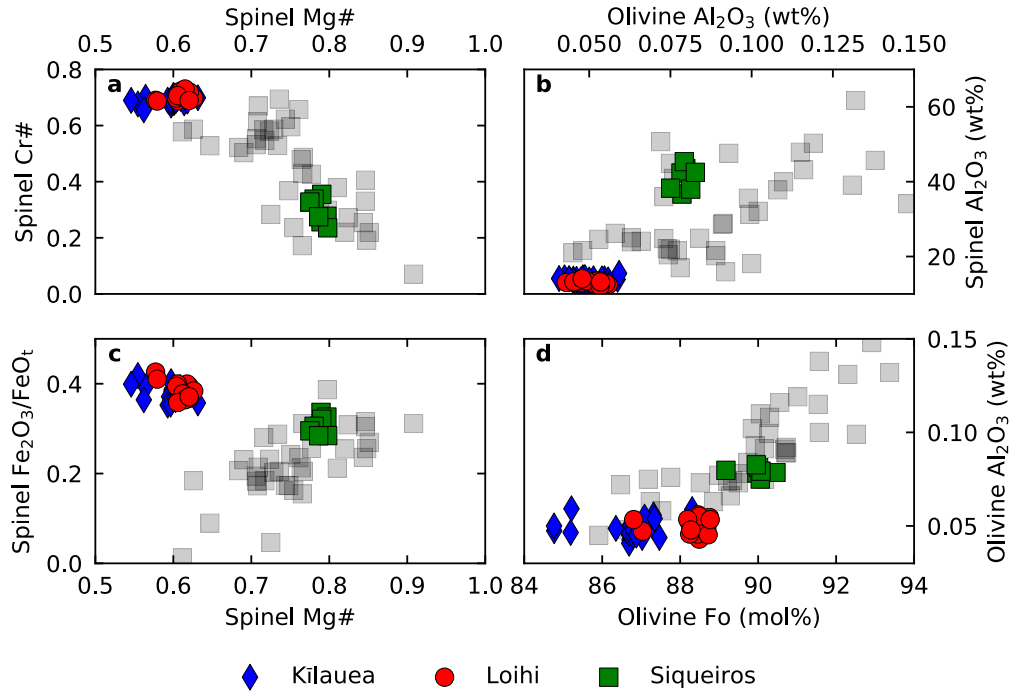
374 *2.1.2 Quantitative element analysis*

375 Quantitative analyses were performed in a single session using a 15 kV beam focused
 376 to $1\ \mu\text{m}$ at 100 nA for olivine and 40 nA for spinel. Calibration was performed using natural
 377 and synthetic standards (Supporting Table S.1.). Instrument drift, precision and accuracy
 378 were monitored by regular analysis of natural secondary standard materials (Supporting
 379 Data Set S.1.). Counting times and crystals used are detailed in Supporting Table S.2.

380 The analytical setup achieved Al detection limits better than 23 ppm, significantly
 381 lower than the measured Al concentrations. Repeat analyses of the Al_2O_3 concentration in
 382 San Carlos olivine showed a 1 s.d. precision of 20 ppm, lower than the combined precision
 383 and accuracy of 25–30 ppmw estimated from counting statistics, which was propagated to
 384 the error in T_{crys} . Spinel $\text{Fe}^{3+}/\text{Fe}_T$ was calculated from the electron probe data following
 385 the method of Droop (1987).

386 **3 Thermometry Results**

387 The composition of the olivine-spinel pairs is summarized in Figure 4, and the dataset
 388 is provided in Supporting Data Set S.2. The composition of the Hawaiian and Siqueiros
 389 olivine crystals (Figure 4d) overlap with the compositions of crystals used to calibrate the
 390 thermometer by Coogan et al. (2014). The Siqueiros spinels have compositions very similar
 391 to the experimental crystals. The Hawaii spinels are offset to lower Mg#, lower Al_2O_3
 392 concentration, and higher $\text{Fe}_2\text{O}_3/\text{FeO}_T$ than the experimental crystals, but have similar



396 **Figure 4.** Summary of the compositions of the olivine and spinel crystals from Hawaii (Kilauea
 397 and Loihi) and Siqueiros analysed in this study. The grey squares show the composition of olivine
 398 and spinel crystals used to calibrate the thermometer by Coogan et al. (2014). Uncertainties are
 399 smaller than the size of the symbols.

393 Cr# to the highest Cr# experimental spinels. These offsets between natural and experi-
 394 mental spinels are small, suggesting the thermometer calibration may still be applied with
 395 confidence.

400 Olivine-spinel pairs from Hawaii record temperatures from $1282 \pm 21^\circ\text{C}$ to $1375 \pm 19^\circ\text{C}$
 401 (Figure 2). The mean crystallization temperature for Loihi, 1345°C , is higher than that for
 402 Kilauea, 1326°C (the standard errors in the means are 4°C and 5°C , respectively). This
 403 small difference in mean crystallization temperature arises from the slightly lower Al₂O₃
 404 concentration in Loihi spinels (Figure 4b). Where multiple spinel inclusions were analysed
 405 within the same host crystal, most recorded identical T_{crys} within error; the few that did
 406 not were most likely entrapped at different stages of magma evolution.

407 The lower mean crystallization temperature of Kilauea olivines coincides with a lower
 408 mean olivine Fo, consistent with being derived from more evolved magmas. However, within
 409 each subpopulation there is substantial crystallization temperature variability and no cor-
 410 relation with olivine composition; the implications of which, for inferring mantle T_p , are
 411 discussed in Section 4.

412 The Siqueiros olivine-spinel pairs record crystallization temperatures from $1270 \pm 16^\circ\text{C}$
 413 to $1289 \pm 17^\circ\text{C}$, higher than, but within uncertainty of, the highest values obtained by Coogan
 414 et al. (2014). This small difference in Siqueiros olivine crystallization temperatures may
 415 reflect a small inter-lab bias in the EPMA analyses, or the crystals used in the two studies
 416 may represent different crystal populations.

4 Identifying crystallization temperatures of primitive basalts

The temperature at which a magma first starts to crystallize olivine, $T_{\text{crys}}^{\text{primary}}$, is likely very close to the temperature at which it arrived in the magma chamber (Matthews et al., 2016). Olivine crystals then continue to form at progressively lower temperatures as the magma cools. When comparing datasets it is important to ensure variations in magmatic evolution are not aliased with the mantle signal. Fortunately, olivine composition closely tracks magmatic evolution, with the most primitive crystals being the most forsteritic. We assume, therefore, that olivines of composition $\text{Fo}_{\geq 91}$ provide the most reliable record of $T_{\text{crys}}^{\text{primary}}$.

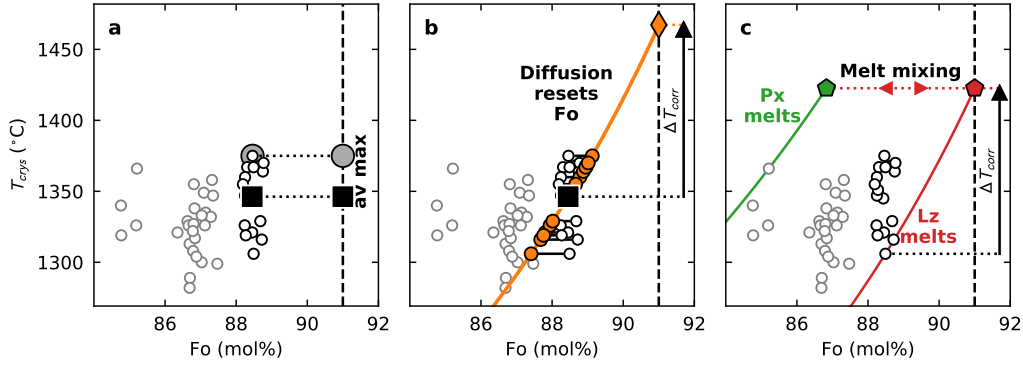
Many datasets exhibit substantial variability in T_{crys} within their high forsterite populations (Figure 2 and Supplementary Figures S.2 and S.3). Variability in T_{crys} that does not correlate with Fo might arise from crystallization of chemically heterogeneous magmas (Matthews et al., 2016, and Section 4.2) or diffusive re-equilibration of Mg and Fe with surrounding crystals and melt (Jennings et al., 2019, and Section 4.1), implying the highest T_{crys} is most representative of $T_{\text{crys}}^{\text{primary}}$. Alternatively, the variability might be ascribed to analytical imprecision and variable attainment of Al-equilibrium between olivine and spinel. In this case, the mean T_{crys} of the high forsterite population is the most appropriate estimate of $T_{\text{crys}}^{\text{primary}}$. We take the conservative approach of taking the mean of the high forsterite, high T_{crys} , population as our estimate of $T_{\text{crys}}^{\text{primary}}$ for such eruptions, as opposed to taking simply the highest T_{crys} value.

Whether or not the most forsteritic olivines are present in erupted material depends on the unique dynamics of individual magmatic plumbing systems; consequently, many eruptions contain only a more evolved crystal cargo. Some of the datasets we invert for mantle T_p , including our new data from Hawaii, do not contain $\text{Fo}_{\geq 91}$ crystals with spinel inclusions. The role of magmatic evolution and coeval cooling must, therefore, be considered when obtaining $T_{\text{crys}}^{\text{primary}}$ from such datasets. One approach is to consider the T_{crys} of evolved olivines as a robust minimum bound on the primary crystallization temperature $T_{\text{crys}}^{\text{primary}}$. However, for a meaningful comparison, the true $T_{\text{crys}}^{\text{primary}}$ should be estimated from the observed Fo- T_{crys} systematics.

The combination of olivine composition and its crystallization temperature can be used to uniquely determine the mole fractions of Mg and Fe in its parental melt (Roeder & Emslie, 1970). A liquid line of descent may then be calculated by the iterative application of a reverse-crystallization algorithm. First, a small amount of the olivine in equilibrium with this melt is added to the melt composition. Second, the temperature at which the new magma composition is olivine-saturated is found, and the new equilibrium olivine composition is identified. These steps are then repeated until the magma is in equilibrium with the most forsteritic olivine assumed to have crystallised from the melts. The methodology for these reverse-crystallization calculations, and the assumptions they require, are detailed in Supporting Text S1.

When employing this method, we must assume the magmas are sufficiently primitive that olivine and spinel are the only phases on the liquidus, and that the proportion of spinel crystallising is sufficiently small to have little effect on the magma composition. We must also make a decision about which olivine composition and T_{crys} value provide the most appropriate starting point for the calculation. Which olivine should be chosen depends on whether diffusive resetting of Fo (Section 4.1) or crystallization from heterogeneous melts (Section 4.2) is responsible for the decoupling of Fo and T_{crys} . To assess the effect of our assumptions about estimating $T_{\text{crys}}^{\text{primary}}$, we use $T_{\text{crys}}^{\text{primary}}$ values calculated assuming both endmembers in our inversions for mantle T_p (Section 6).

Another prerequisite for estimating $T_{\text{crys}}^{\text{primary}}$ with this method is knowing the value of equilibrium-olivine Fo at which the liquid line of descent extrapolation should be terminated. The most forsteritic olivine crystallized is likely to vary between locations (e.g.,



474 **Figure 5.** Three possible approaches to estimating the crystallization temperature of primitive
 475 melts from the distribution of the Hawaiian olivine-spinel crystallization temperatures. Only the
 476 most forsteritic sub-population is included in the calculations (shown by the circles with darker
 477 outlines). Panel a demonstrates an approach taking the average and maximum crystallization
 478 temperatures present. Panel b shows the result of extrapolating a liquid line of descent from
 479 the average crystallization temperature and olivine composition to Fo₉₁ olivine, as would be in
 480 equilibrium with lherzolithic mantle. Panel c shows how two liquid lines of descent from melts of
 481 different composition bound the population of olivine crystals.

468 Figure 2; Putirka, 2005; Putirka et al., 2007, 2018). Whilst we could correct back to the
 469 most forsteritic crystal observed in each location, as done by Putirka (2005); Putirka et al.
 470 (2007, 2018), we cannot be certain that olivine crystals with higher forsterite contents were
 471 crystallised, but not erupted. For simplicity, we extend the liquid lines of descent back to
 472 Fo₉₁ olivine in all correction calculations; any uncertainty introduced by this assumption
 473 being negligible compared to the uncertainty in which correction method should be applied.

482 4.1 Diffusive resetting

483 Diffusive re-equilibration of a crystal pile of variably forsteritic olivines will progres-
 484 sively shift the Fo of each crystal towards the population mean (Thomson & MacLennan,
 485 2012). The slow diffusion of Al through olivine means that the original olivine Al concentra-
 486 tion is likely to be retained (Coogan et al., 2014). It follows that the discrepancy in diffusion
 487 rates can efficiently decouple T_{cryst} from Fo in a population of olivine crystals. If the initial
 488 diversity of Fo and T_{cryst} were derived from the fractional crystallization of a single magma,
 489 the population mean Fo and T_{cryst} will fall very close to the liquid line of descent (Figure 5b),
 490 making it an appropriate starting composition to use for calculating $T_{\text{cryst}}^{\text{primary}}$.

491 When a population of olivine crystals is derived from fractional crystallization of a
 492 single magma, followed by partial diffusive re-equilibration in a closed system, the highest
 493 values of T_{cryst} will be found only in crystals more forsteritic than the population mean,
 494 and the lowest values of T_{cryst} only in less forsteritic olivines. The Hawaii dataset does
 495 not exhibit this pattern (Figure 5). However, the diversity of melt inclusion trace element
 496 ratios demonstrate that the Kilauea olivines are not derived from fractional crystallization
 497 of a single magma (Sides et al., 2014b; Wieser et al., 2019), we should therefore not expect
 498 crystals to conform to diffusive re-equilibration from a single liquid line of descent. Diffusion
 499 is still a plausible mechanism for generating the Fo- T_{cryst} decoupling in the Hawaii dataset,
 500 but could be acting in addition to magma mixing (Section 4.2).

501 The predicted Fo- T_{crys} pattern, i.e., a steepening of a single liquid line of descent (the
 502 orange line in Figure 5b), is also not seen in any of the other datasets we invert in Section 6
 503 (Supplementary Figures S.2 and S.3). If crystals are derived from fractional crystallization
 504 of a single magma, the non-appearance of this pattern in natural data might reflect crystal
 505 scavenging on a significantly different length scale than the diffusion length scale. Whilst the
 506 datasets do not conform to the simplest permutation of diffusive homogenization, we think
 507 it unlikely that the olivine population mean is displaced significantly from its primary value
 508 (assuming diffusion is responsible for the decoupling); however, making this assumption does
 509 introduce unquantifiable uncertainty into the value of $T_{\text{crys}}^{\text{primary}}$ used for the T_p inversions in
 510 Section 6.

511 4.2 Concurrent magma crystallization and mixing

512 Olivine populations in Fo- T_{crys} space can be bounded by two liquid lines of de-
 513 scent (LLD) (Figure 5c) each corresponding to a primary magma of distinct composition
 514 (Matthews et al., 2016). Pyroxenite-derived melts generally have a lower Mg# and a higher
 515 FeO content than lherzolite-derived melts (e.g., Kogiso et al., 2004; Lambart et al., 2009;
 516 Jennings et al., 2016); therefore, they will saturate in olivine of lower Fo at the same temper-
 517 ature, compared to lherzolite-derived melts (Roeder & Emslie, 1970). Since the lherzolite-
 518 derived melts are the most likely to have been in equilibrium with Fo $_{\geq 91}$ olivine, the most
 519 suitable starting point for extrapolating back to $T_{\text{crys}}^{\text{primary}}$ is an olivine crystallized on the
 520 lherzolite-derived melt LLD. The lower bounding liquid line of descent in Fo- T_{crys} space
 521 represents olivines crystallized from melts closest to the lherzolite-derived endmember, and
 522 so the termination of this LLD at Fo $_{91}$ defines our estimate for $T_{\text{crys}}^{\text{primary}}$.

523 By assuming the apparent decoupling between Fo and T_{crys} arises from primary magma
 524 heterogeneity, a lower $T_{\text{crys}}^{\text{primary}}$ estimate will be obtained than would be obtained by assum-
 525 ing a diffusive origin for the decoupling (Section 4.1). During crustal residence, magma
 526 diversity is gradually homogenised (A. Sobolev & Shimizu, 1994; Saal et al., 1998; MacLen-
 527 nan, 2008; Shorttle, 2015; Shorttle et al., 2016), meaning the range in T_{crys} should become
 528 tighter with decreasing Fo. Whilst the crystallization temperature dataset from Iceland is
 529 consistent with this (Figure 2 and Matthews et al., 2016), the same feature is not obvious in
 530 other datasets. The lack of a progressive mixing signal in these other datasets might be due
 531 to each spanning an insufficient range of olivine Fo, or the signal may have been modified
 532 by diffusive Fo re-equilibration.

533 5 Modelling mantle melting

534 Linking $T_{\text{crys}}^{\text{primary}}$ to mantle T_p requires quantification of the latent heat of melting.
 535 To this end we employ a model for multi-lithologic adiabatic mantle melting which allows
 536 us to predict $T_{\text{crys}}^{\text{primary}}$ for specified mantle T_p , pyroxenite fraction, ϕ_{px} , and harzburgite
 537 fraction, ϕ_{hz} . Using a melting model enables simultaneous prediction of observable proxies
 538 for magma productivity: crustal thickness at oceanic spreading centres and magma flux at
 539 ocean islands. Here we summarize the melting model and how it is applied to spreading-
 540 ridge and intra-plate magmatism. In Section 6 we describe how we invert the model to
 541 estimate mantle T_p and its uncertainty from $T_{\text{crys}}^{\text{primary}}$.

542 Our models are based on the generalized formulation by Phipps Morgan (2001) for
 543 calculating the melting behaviour of a multi-component mantle during adiabatic decompres-
 544 sion. Any mantle lithology may be incorporated into this framework, provided expressions
 545 exist for the partial derivatives of temperature, T , with melt fraction, F , and pressure, P ,
 546 $(\frac{\partial T}{\partial F})_P$ and $(\frac{\partial T}{\partial P})_F$ (the subscript indicates which parameter is kept constant), the entropy
 547 change on melting, ΔS , the heat capacity, C_p and density, ρ . The reader is referred to
 548 Phipps Morgan (2001) and Shorttle et al. (2014) for a full description of the model, and
 549 to Matthews et al. (2016) for a thorough characterization of its behaviour when predicting

550 crystallization temperatures. Here we provide an overview of the most important features
551 of the model, and how it is applied to mid-ocean ridge and intra-plate magmatism.

556 First, the geotherm through the melting region must be calculated. The path of the
557 geotherm depends on the mantle T_p and the melt fraction, which itself is controlled by ϕ_{px}
558 and ϕ_{hz} , and the properties of each lithology listed in the preceding paragraph. The forward
559 model found to provide the best fit to the Hawaii $T_{\text{cryst}}^{\text{primary}}$ is shown in Figure 6. Prior to
560 crossing its solidus, upwelling mantle follows the solid adiabat, losing heat only to the work
561 done during expansion. Once the mantle crosses the pyroxenite solidus it begins melting
562 (blue line in Figure 6b), heat is extracted by the latent heat of melting, causing the mantle
563 temperature to decrease more rapidly per unit of decompression. Upon further upwelling
564 the mantle crosses the lherzolite solidus (purple line in Figure 6b), increasing the rate of
565 melting, and causing the temperature to decrease more rapidly still. Following Shorttle et
566 al. (2014) and Matthews et al. (2016), we assume the harzburgite fraction does not melt.

577 Melting ceases once the mantle reaches the base of the lithosphere (the tan-shaded
578 region in Figure 6b), and the melt is extracted to a magma chamber (shown by the diamond
579 symbol), which we assume to lie at the base of the crust. Whilst crystallization takes
580 place throughout the crust (e.g. Cashman et al., 2017; Neave & Putirka, 2017) and in
581 the lithospheric mantle underlying the crust (e.g., Kelemen et al., 1997; Herzberg, 2004),
582 the uncertainty this introduces is difficult to quantify, but we think it most likely that the
583 primitive crystals we consider here crystallize close to the base of the crust. As no further
584 melt is generated, and we assume the melt does not interact with the lithosphere, the rate
585 of temperature change from this point follows the liquid adiabat. Finally, the temperature
586 of olivine saturation is calculated. A magma will saturate at a temperature determined by
587 both its composition and the pressure. Putirka (2008b) provides a simple expression (Eq.
588 15) for this relationship, modified from Helz and Thornber (1987). Following Matthews et
589 al. (2016) we use the pressure dependence of this expression to extrapolate from the pressure
590 and temperature at which a magma leaves the mantle, to the temperature at which it will
591 begin to crystallise at lower pressure. If this saturation temperature is cooler than the
592 temperature at which the melt arrives, the melt must lose heat before crystallizing olivine.
593 This final step is not visible on Figure 6 as the temperature of olivine saturation is very
594 close ($< 10^\circ\text{C}$) to the temperature at which we predict the melts to arrive in the magma
595 chamber.

596 The melt fraction of each lithology is calculated simultaneously with the geotherm
597 (Figure 6c). The total melt fraction (grey in 6c) is lower than the melt fractions of the
598 lherzolite and pyroxenite (blue and purple, respectively) since, in this solution, we find a
599 considerable amount of non-melting harzburgite to be present.

600 When melting occurs at spreading-ridges by passive upwelling, the crustal thickness
601 can be calculated directly from the total melt fraction, F , (White et al., 1992), without
602 knowledge of the upwelling velocities or the detailed melting region geometry:

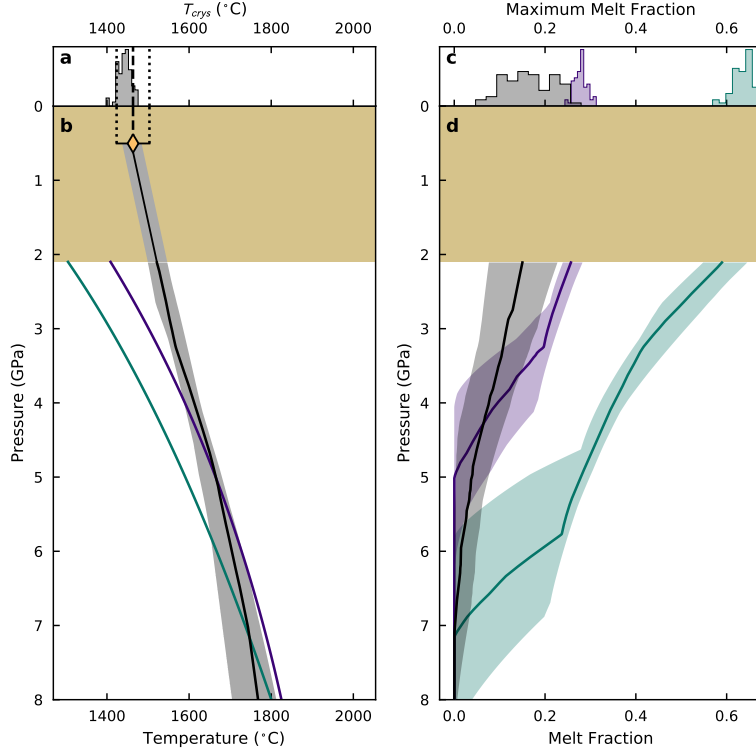
$$t_{\text{crust}} = \frac{1}{\rho g} \int_{P_0}^{P_l} \frac{F}{1-F} dP, \quad (4)$$

603 where ρ is the density of crust, g is the gravitational acceleration, and P_l and P_0 are the
604 pressures at the base of the lithosphere and onset of melting, respectively. The contribution
605 of pyroxenite-derived melts to the volume of the crust can be calculated using a similar
606 expression:

$$X_{\text{px}} = \frac{\int_{P_0}^{P_l} \frac{F_{\text{px}}}{1-F} dP}{\int_{P_0}^{P_l} \frac{F}{1-F} dP}, \quad (5)$$

607 where F_{px} is the melt fraction of the pyroxenite.

608 In settings where mantle decompression is caused by plume-driven (active) upwelling,
609 melt thicknesses or fluxes can be calculated, provided the mantle upwelling velocity and



552 **Figure 6.** Illustration of the forward models representing the median and 95% confidence intervals for Hawaii, found by inverting $T_{\text{crys}}^{\text{primary}}$ and magma flux, Q_m . Panel a shows the distribution of crystallization temperatures recovered from the inversion results. Panel b shows the thermal structure of the melting region. The lherzolite and pyroxenite solidi are shown by the purple and blue lines. Panel c shows the distribution of maximum lherzolite (purple), pyroxenite (green-blue) and total mantle melt (grey) fractions. The total melt fraction may be less than both the lherzolite and pyroxenite melt fractions when (non-melting) harzburgite is included in the calculation. Panel d shows the evolution with pressure of each lithology's melt fraction. In both panels b and d, the lithosphere is shown by the tan shading. The diamond symbol and error bars in panel b show the value of $T_{\text{crys}}^{\text{primary}}$ estimated with the diffusive end-member correction (Section 4.1), placed at the pressure corresponding to the base of the crust. Note that the geotherms and melt fractions vs depth curves are shown for fixed lithosphere thickness and magma chamber depths, in reality each solution has its own lithosphere thickness and magma chamber depth, their distribution controlled by their uncertainties.

610 melting region geometry is known. Shorttle et al. (2014) made the simplifying assumption
 611 that plume flow approximates flow through a deformable conduit, applying the expression
 612 from Turcotte and Schubert (2014):

$$Q_v = \frac{\pi}{8} \frac{\Delta\rho g r^4}{\mu_p} \quad (6)$$

613 where Q_v is the volume flux of mantle, $\Delta\rho$ is the density difference between the mantle
 614 plume and ambient mantle, g is the gravitational acceleration, r is the conduit radius, and
 615 μ_p is the viscosity of the plume. In applying this equation we are neglecting the effect
 616 of the overlying lithosphere on the velocity field of the upwelling mantle: by the time the
 617 plume material reaches the base of the lithosphere its vertical velocity must be zero. Our
 618 approach will, therefore, lead to us over-estimating melt production, as a non-diminishing
 619 upwelling velocity will cause more decompression melting than the real case. Increased melt
 620 production means a greater amount of heat is extracted by melting; consequently, melts
 621 will leave the mantle and crystallise at a lower temperatures. This simplification means our
 622 inversion results will be biased towards slightly higher values of T_p in locations where we
 623 constrain the results using magmatic flux.

624 $\Delta\rho$ is taken to be the density difference at 80 kbar, and is calculated from the weighted
 625 average of the lithology densities at the appropriate T_p . The density of each lithology is
 626 calculated using THERMOCALC v3.40 (Powell et al., 1998) with the dataset from Holland
 627 and Powell (2011) and the solution models by Jennings and Holland (2015). The value of
 628 μ_p is set to 10^{19} Pas as a conservative, low, estimate of mantle viscosity (Shorttle et al.,
 629 2014), biasing the inversion towards predicting high volume fluxes, lower F , and therefore
 630 lower mantle T_p . To convert the plume volume flux to a melt flux Q_m , we multiply Q_v by
 631 the total melt fraction at the top of the melting region, assuming the densities of solid and
 632 melt are comparable within the uncertainties of the calculation.

633 Modelling the highest values of mantle T_p inferred throughout Earth's history (e.g.,
 634 the Galápagos plume-related lavas studied by Alvarado et al., 1997; Trela et al., 2017)
 635 and characterising the high T_p tail of the inverted T_p probability distributions (Section
 636 6), requires melting at pressures far in excess of 10 GPa. The models presently available
 637 for lherzolite melting (e.g., Katz et al., 2003; Hirschmann, 2000; Herzberg et al., 2000)
 638 and pyroxenite melting (e.g., Shorttle et al., 2014; Lambart et al., 2016; Pertermann &
 639 Hirschmann, 2003) are typically calibrated on experiments run at pressures of 10 GPa and
 640 lower. Even if the expressions were to be extrapolated beyond their calibrated range, the use
 641 of quadratic functional forms for the solidus and liquidus (e.g., Katz et al., 2003; Shorttle
 642 et al., 2014) means extrapolation rapidly becomes not only inaccurate, but unphysical, as
 643 melting pressures exceed the stationary points of the functions.

644 To enable us to model high values of mantle T_p we take two approaches. First, we
 645 calibrate new parameterizations of lherzolite and pyroxenite melting suitable for calcula-
 646 tions up to at least 10 GPa. In Supporting Text S2, we provide models for melting of the
 647 silica-undersaturated pyroxenite KG1, a silica-oversaturated pyroxenite, and KLB-1 lherzo-
 648 lite. Putirka et al. (2007) and Putirka (2016) also took this approach to calculating melting
 649 behaviour at high pressures, calibrating new functions for the lherzolite liquidus and solidus.
 650 Whilst the Katz et al. (2003) parameterization for lherzolite melting can be used at pressures
 651 up to 10 GPa, a wide range of peridotite compositions is used in its calibration, including
 652 silica-undersaturated pyroxenites, which we model here as a separate lithology. In all the
 653 inversions in Section 6, we use the silica-undersaturated pyroxenite as the pyroxenite end-
 654 member. Secondly, we introduce an isobaric melting step for calculations where the solidus
 655 is intersected at pressures greater than 10 GPa, the expressions for which are provided in
 656 Supporting Text S5.

6 Inverse model

The forward model allows us to predict the value of $T_{\text{crys}}^{\text{primary}}$ for given values of mantle T_p , ϕ_{px} , ϕ_{hz} , lithosphere thickness and magma chamber depth. However, it is the inverse calculation that is of most interest, i.e., predicting the value of T_p given an observation of $T_{\text{crys}}^{\text{primary}}$, subject to the uncertainties of the other parameters. For some localities we have additional observations which can constrain mantle T_p : the crustal thickness t_{crust} at mid-ocean ridges, equivalently the magmatic flux, Q_m , at intra-plate volcanic centres, and the fraction of pyroxenite derived melt X_{px} . The parameters t_{crust} , Q_m , and X_{px} can be simultaneously calculated from the forward model (Section 5).

To find the set of solutions which can reproduce $T_{\text{crys}}^{\text{primary}}$, and other constraints where applicable, we use a Bayesian Monte Carlo inversion routine, summarised in Figure 1. A large number of forward models are run with values for each required parameter chosen according to the prior probability distributions we define. The fit of each model to the data is assessed with the log-likelihood function, $\ln(L)$, and the estimates of all the model parameters are refined. This process is repeated until the maximum likelihood region is sufficiently characterized for estimation of the posterior probability distributions of each parameter. We implement the MultiNest Monte Carlo nested sampling algorithm (Feroz & Hobson, 2008; Feroz et al., 2009, 2013) using the pyMultiNest wrapper (Buchner et al., 2014).

For each parameter x that the inversion is required to match, the contribution to the log-likelihood is given by:

$$\ln(L) = \sum_x \ln(L_x), \quad (7)$$

$$\ln(L_x) = -\frac{1}{2} \ln(2\pi\sigma_x^2) - \frac{(x_{\text{obs}} - x_{\text{calc}})^2}{2\sigma_x^2}, \quad (8)$$

where x_{obs} is the observed value, σ_x is its standard deviation, and x_{calc} is the value predicted by the forward model.

Whilst it is possible, in principle, to match the observations of $T_{\text{crys}}^{\text{primary}}$, t_{crust} , and Q_m with extremely high fractions of pyroxenite, in such a scenario the mantle is unlikely to be buoyant with respect to the ambient mantle (Shorttle et al., 2014). Where intra-plate magmatism is thought to be generated within a buoyantly rising mantle plume, such solutions are not physically realistic. To prevent negatively buoyant solutions contributing to the posterior probability distributions, we modify the likelihood function when $\rho_{\text{plume}} > \rho_{\text{ambient}}$:

$$\ln(L_{\text{buoyancy}}) = \ln(L) - (\exp(\rho_{\text{plume}} - \rho_{\text{ambient}}) - 1), \quad (9)$$

where the density difference is calculated at 80 kbar.

In addition to Hawaii, we apply the same inversion to a number of locations with published olivine-spinel aluminum-exchange T_{crys} estimates, the literature sources of which are shown in Table 1. We only include locations where estimates of the lithospheric thickness at the time of the igneous activity have been made. We also repeat the calculations made by Matthews et al. (2016) for Iceland and Siqueiros using our new parameterizations of mantle melting and data from Siqueiros.

Following Matthews et al. (2016), we use the crustal thickness at Iceland's coast to further constrain mantle T_p . Though Iceland lies above a mantle plume, MacLennan et al. (2001) demonstrated that active mantle-upwelling is not required to explain the composition or volume of magmatism at Iceland's coasts. The Icelandic melting region may, therefore, be treated as passive upwelling beneath a mid-ocean ridge. We also use X_{px} for both Iceland and Siqueiros, which have estimated X_{px} from magma chemistry (Shorttle et al., 2014; Hirschmann & Stolper, 1996). We do not use X_{px} to constrain solutions for the intra-plate settings, as its value is very sensitive to assumptions about melting region geometry.

Location	T_{cryst}^* ($^{\circ}\text{C}$)	t_{lith} (km)	t_{crust} (km)	X_{px}	Q_m (m^3s^{-1})	refs
Hawaii (diff.)	1464 \pm 20 ^a	75 \pm 5	18 \pm 1		10 \pm 2	1,2,3,4
Hawaii (het.)	1419 \pm 20 ^a	75 \pm 5	18 \pm 1		10 \pm 2	1,2,3,4
Iceland	1383 \pm 22	–	20 \pm 1	0.3 \pm 0.1		5,6,7
Siqueiros	1280 \pm 20	–	5.74 \pm 0.27	0.175 \pm 0.1		1,8,9
<i>North Atlantic Igneous Province</i>						
Rum	1462 \pm 22	70 \pm 5	28 \pm 2			10,11,12
Skye	1465 \pm 22	70 \pm 5	28 \pm 2			10,11,12
Mull	1400 \pm 22	70 \pm 5	28 \pm 2			10,11,12
Baffin	1413 \pm 22	60 \pm 5	35 \pm 1			10,13,14
SE Greenland	1398 \pm 22 ^a	60 \pm 5	27 \pm 2			15,11,16
W Greenland	1421 \pm 22	60 \pm 5	33 \pm 2			10,13,16
<i>Caribbean Large Igneous Province</i>						
Curaçao	1353 \pm 20 ^a	60 \pm 10	30 \pm 5 ^b			17,18
Gorgona	1403 \pm 22	60 \pm 10	30 \pm 5 ^b			15,18
Tortugal	1578 \pm 20	60 \pm 10	30 \pm 5 ^b			17,18
<i>Other Large Igneous Provinces</i>						
Karoo	1471 \pm 35	45 \pm 5	30 \pm 5 ^b			19,11
Emeishan	1438 \pm 32	60 \pm 5	30 \pm 5 ^b			20,21
Etendeka	1469 \pm 24	50 \pm 10	20 \pm 2			22,23,24

711 **Table 1.** References: 1. This study. 2. Putirka (1999); Bock (1991). 3. Watts and Ten Brink
712 (1989). 4. Wessel (2016). 5. Matthews et al. (2016). 6. Darbyshire et al. (2000). 7. Shorttle et
713 al. (2014). 8. Aghaei et al. (2014). 9. Hirschmann and Stolper (1996). 10. Spice et al. (2016). 11.
714 White and M^cKenzie (1995). 12. Davis et al. (2012). 13. Gill et al. (1992). 14. Gilligan et al.
715 (2016). 15. Coogan et al. (2014). 16. Kumar et al. (2007). 17. Trela et al. (2017). 18. Kerr (2005).
716 19. Heinonen et al. (2015). 20.R. Xu and Liu (2016). 21. Y. Xu et al. (2001). 22. Jennings et al.
717 (2019). 23. Thompson and Gibson (2000). 24. Thompson et al. (2001). *The values for T_{cryst} shown
718 here are for the inversions shown in Figure 7, a full list of the T_{cryst} values used in all inversions is
719 given in Supporting Table S.3. ^aValue has been corrected for fractional crystallization back to Fo_{91}
720 using the diffusion correction, unless indicated. ^bSince the lavas are located on accreted terrains,
721 and the inversion is very weakly sensitive to t_{crust} , a value is assumed.

703 The only location where Q_m is used to constrain the solution is Hawaii, as there is
704 little constraint on the geometry of the melting region beneath LIPs at the time of their
705 formation. Hence, we choose values for the plume conduit radius appropriate for Hawaii:
706 between 50 and 300 km. These bounds are derived from the dynamic models of the Hawaiian
707 plume by Watson and M^cKenzie (1991); the lower bound corresponding to the radius of the
708 melting region, and the upper bound to the radius of plume-driven upwelling. This range
709 of values propagates both the uncertainty associated with the dynamic models, and the
710 uncertainty generated by assuming the radial temperature field is uniform.

722 The lithosphere thickness, t_{lith} , determines when melting ceases. For the North At-
723 lantic Igneous Province we use estimates made by Hole and Millett (2016) using the PRIMELT3
724 algorithm (Herzberg & Asimow, 2015). For both Rum and Skye, Hole and Millett (2016)
725 calculate two different final melting pressures. We use the higher of the two estimates for
726 both locations as the samples for which thermometry was performed come from early in
727 the magmatic activity, when the lithosphere was likely to be at its thickest. The base of

728 the lithosphere for Iceland and MORB is taken as the base of the crust, calculated by the
 729 model. The priors for t_{lith} and the magma storage pressure (taken to be the base of the
 730 crust, t_{crust}) are normal distributions defined by their estimated value and its uncertainty
 731 (Table 1).

732 The priors set on ϕ_{px} and ϕ_{hz} are both uniform distributions from 0 to 1. Though
 733 this provides a uniform probability distribution over $\phi_{\text{lz}} - \phi_{\text{px}} - \phi_{\text{hz}}$ space, half of the solutions
 734 (where $\phi_{\text{px}} + \phi_{\text{hz}} > 1$) are not physical. A crude, but effective, approach we adopt to prevent
 735 such unphysical solutions, is to return the following log-likelihood value when $\phi_{\text{px}} + \phi_{\text{hz}} > 1$:

$$\ln(L) = -10^{10} \exp(1 + \phi_{\text{px}} + \phi_{\text{hz}}) \quad (10)$$

736 For locations with $\text{Fo}_{\geq 91}$ olivine crystals, we use the mean of the high T_{crys} population
 737 as our estimate for $T_{\text{crys}}^{\text{primary}}$, shown in Supplementary Figures S.2 and S.3. Where locations
 738 lack $\text{Fo}_{\geq 91}$ olivine crystals, we apply the correction methods described in Section 4. Inver-
 739 sions are run using $T_{\text{crys}}^{\text{primary}}$ estimates derived from both correction schemes, in addition
 740 to the uncorrected mean T_{crys} . The parameters used in the correction calculations, and
 741 their results, are shown in Supporting Table S.3. Table 1 shows only the $T_{\text{crys}}^{\text{primary}}$ estimates
 742 derived from the diffusive correction.

733 7 Inversion results and discussion

744 The values of mantle T_p calculated for Hawaii and the other locations in our compi-
 745 lation are summarized in Figure 7 and Table 2. The best fit geotherms and melt fractions
 746 for each locality are shown in Supporting Figures S.6 to S.22. The marginal likelihood
 747 distributions are shown in Supporting Figures S.23 to S.41, and summarised in Supporting
 748 Table S.4. Values of t_c , X_{px} , and Q_m calculated from the posterior distributions are shown
 749 in Supporting Figures S.42 to S.45, the values of $T_{\text{crys}}^{\text{primary}}$ calculated from the posterior
 750 distributions are shown in Supporting Figures S.6 to S.22, and are all summarised in Sup-
 751 porting Table S.5. In all cases, the constraints are adequately reproduced by the posterior
 752 distributions.

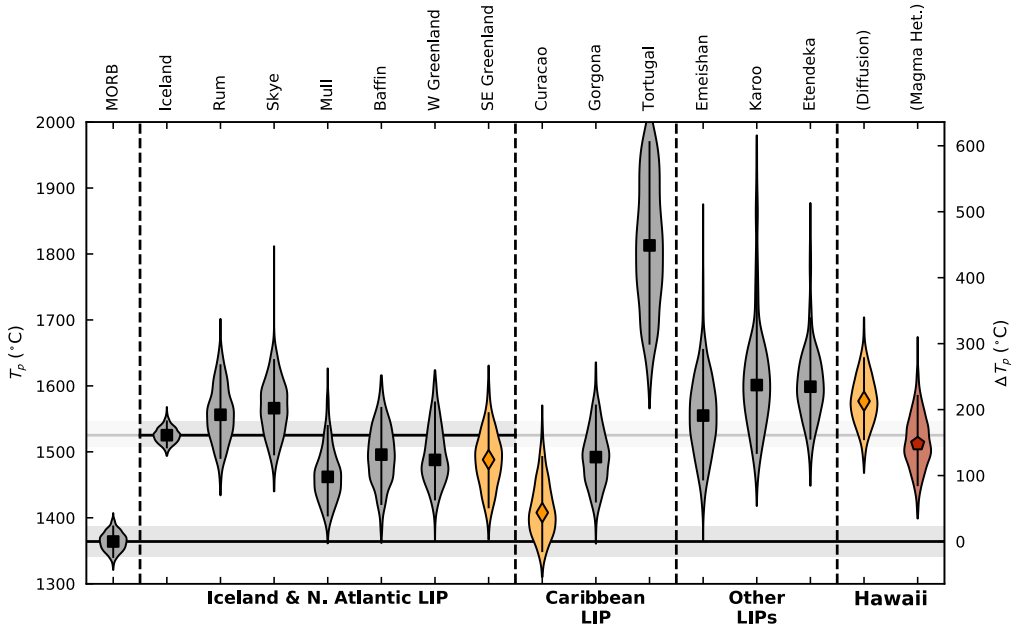
764 All plume localities, except Curaçao, have mantle T_p significantly higher than MORB
 765 (Siqueiros, 1364_{-23}^{+23} °C). Whilst there is substantial variability in maximum-likelihood T_p
 766 among plume locations, most of the posterior distributions overlap with the Iceland posterior
 767 distribution. The posterior T_p distribution for Tortugal is an exception to this, suggesting
 768 that crystallization temperatures do, most likely, record variable mantle plume T_p . Figure
 769 8 allows assessment of whether our choices of lithosphere thickness t_{lith} , magma chamber
 770 depth t_{crust} , and $T_{\text{crys}}^{\text{primary}}$ introduce systematic biases into our T_p estimates. No co-variation
 771 between these variables and T_p is observed, save for $T_{\text{crys}}^{\text{primary}}$, implying our choices of t_{lith}
 772 and t_{crust} do not systematically bias our results.

780 The strong covariation of $T_{\text{crys}}^{\text{primary}}$ with T_p (Figure 8a) demonstrates the median of the
 781 posterior T_p distribution is primarily controlled by $T_{\text{crys}}^{\text{primary}}$. The strong correlation between
 782 $T_{\text{crys}}^{\text{primary}}$ and T_p might suggest direct comparison of $T_{\text{crys}}^{\text{primary}}$ will yield meaningful insights
 783 into mantle T_p variation without further modelling. However, the uncertainty on the T_p
 784 estimates encompasses much of the inter-plume variation. Since much of this uncertainty
 785 is propagated from uncertainty in ϕ_{px} and ϕ_{hz} , only where ϕ_{px} and ϕ_{hz} are thought to be
 786 comparable between two locations, will a direct comparison of $T_{\text{crys}}^{\text{primary}}$ be meaningful.

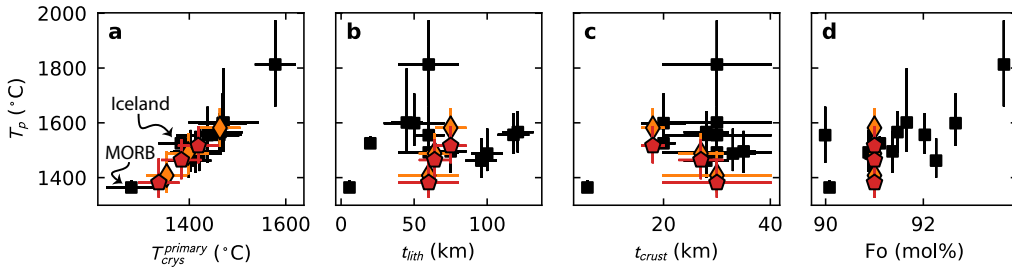
787 Siqueiros (MORB) and Iceland fall off the main trend in Figure 8a, confirming that
 788 tectonic setting plays an important role in determining T_{crys} . The ability of the mantle
 789 to upwell to much shallower levels at mid-ocean ridges than in intra-plate settings means
 790 a greater melt fraction can be achieved, more heat is extracted during melting, and melts
 791 crystallize at systematically lower T_{crys} . Consequently, caution must be exercised when
 792 comparing intra-plate raw T_{crys} values to MORB or Iceland.

Location	High $T_{\text{crys}}/\text{Fo}_{91}$ population ($^{\circ}\text{C}$)	Extrapolated to Fo_{91}	
		Diffusion ($^{\circ}\text{C}$)	Magma Het. ($^{\circ}\text{C}$)
Hawaii (magma flux)	1402 ⁺⁶⁹ ₋₄₅	1582 ⁺⁶⁸ ₋₆₅	1516 ⁺⁶⁷ ₋₅₉
Hawaii	–	1592 ⁺⁶⁶ ₋₈₀	1522 ⁺⁷⁷ ₋₇₇
Iceland	1525 ⁺²¹ ₋₁₈	–	–
Siqueiros (MORB)	1364 ⁺²³ ₋₂₃	–	–
<i>North Atlantic Igneous Province</i>			
Rum	1556 ⁺⁷⁵ ₋₆₅	–	–
Skye	1566 ⁺⁷³ ₋₇₀	–	–
Mull	1462 ⁺⁷⁷ ₋₅₈	–	–
Baffin	1496 ⁺⁷¹ ₋₇₅	–	–
W Greenland	1487 ⁺⁸⁷ ₋₆₀	–	–
SE Greenland	1397 ⁺⁸⁹ ₋₅₂	1488 ⁺⁷⁰ ₋₇₂	1464 ⁺⁷¹ ₋₆₆
<i>Caribbean Large Igneous Province</i>			
Curaçao	1279 ⁺³⁴ ₋₂₃	1408 ⁺⁸⁴ ₋₅₈	1381 ⁺⁸⁴ ₋₅₀
Gorgona	1492 ⁺⁷⁸ ₋₆₇	–	–
Tortugal	1813 ⁺¹⁵⁷ ₋₁₄₉	–	–
<i>Other Large Igneous Provinces</i>			
Emeishan	1555 ⁺¹⁰⁰ ₋₉₇	–	–
Karoo	1601 ⁺¹⁹³ ₋₁₀₃	–	–
Etendeka	1599 ⁺¹⁰⁴ ₋₇₉	–	–

753 **Table 2.** T_p estimates calculated using either raw T_{crys} values (first column), or using $T_{\text{crys}}^{\text{primary}}$
754 values derived using the correction schemes derived in Section 4. The values quoted are the medians
755 of the posterior T_p distributions, and the uncertainties are their 5th and 95th percentiles.



756 **Figure 7.** Estimates of mantle potential temperature (T_p) derived from the means of the high
 757 T_{cryst} populations seen in each location (black squares and grey histograms), or from applying the
 758 correction method assuming diffusive Fo and T_{cryst} decoupling (orange diamonds and histograms).
 759 The right-hand axis shows the T_p offset relative to the median MORB (Siqueiros) T_p estimate. The
 760 horizontal lines show the median T_p estimates for MORB (Siqueiros) and Iceland; the grey shading
 761 shows their 5th and 95th percentiles. For Hawaii, the T_p estimate from applying the magma-
 762 heterogeneity correction scheme is shown (red pentagon and histogram). The inversion results
 763 shown for Hawaii satisfy the observed magma flux. Error bars show the 5th and 95th percentiles.



773 **Figure 8.** Estimates of mantle potential temperature (T_p) compared to the primary crystalliza-
 774 tion temperature ($T_{\text{cryst}}^{\text{primary}}$), the lithospheric thickness (t_{lith}), and crustal thickness (t_{crust}) used in
 775 the inversions (panels a, b and c). Also shown (panel d) is the relationship between T_p estimate
 776 and olivine composition from which $T_{\text{cryst}}^{\text{primary}}$ is derived. Symbols distinguish whether the crystal-
 777 lization temperature used in each inversion was the average of the high temperature population
 778 (black squares), or corrected back to Fo₉₁ (orange diamonds for the diffusive $T_{\text{cryst}}^{\text{primary}}$ correction,
 779 and red pentagons for the magma-heterogeneity $T_{\text{cryst}}^{\text{primary}}$ correction).

793

7.1 Siqueiros (MORB)

794

795

796

797

798

799

800

801

A consequence of using our new parameterizations of mantle melting (Supporting Text S2) is a systematic shift to higher estimates of mantle T_p when compared with the calculations by Matthews et al. (2016). In this study we calculate a mantle T_p for Siqueiros of 1364^{+23}_{-23} °C, higher but within error of 1318^{+44}_{-32} °C calculated by Matthews et al. (2016). In addition to the systematic shift towards higher mantle T_p , we also used a higher value of $T_{\text{crys}}^{\text{primary}}$, derived from our new measurements (Section 3). This systematic offset highlights the importance of making comparisons between mantle T_p estimates derived using the same models.

802

803

804

805

806

807

808

809

810

811

812

We report a lower uncertainty on the Siqueiros mantle T_p than Matthews et al. (2016), a consequence of taking a more robust Bayesian approach to parameter estimation. The uncertainty on our estimate of Siqueiros mantle T_p , alongside the uncertainty on our estimate for Iceland, is much lower than the other locations for which we estimate T_p . This much smaller uncertainty originates from the tight constraint crustal thickness places on the total melt fraction at mid-ocean ridges. The small uncertainty estimate does not include uncertainty in the melting models themselves; model uncertainty will affect all inversion results systematically. Such systematic uncertainty is of little consequence when considering the relative differences in mantle T_p . We also neglect uncertainty in application of the thermometer, i.e. the uncertainty in how close to equilibrium the olivine and spinel are, as this is difficult to quantify.

813

7.2 Iceland

814

815

816

817

818

819

820

As for Siqueiros, our new estimate of the Icelandic mantle T_p (1525^{+21}_{-18} °C) differs from the T_p estimated by Matthews et al. (2016) (1480^{+37}_{-30} °C), but they are within mutual uncertainty. Our new inversions suggest a lower value of ϕ_{Hz} , but it is still significant, and in part reflects the more refractory nature of our new parameterization for lherzolite melting. As discussed by Matthews et al. (2016) the relative temperature offset between Iceland and Siqueiros agrees well with many previous studies, despite the inclusion of lithological heterogeneity in our models.

828

829

830

831

832

833

Figure 9b demonstrates a small positive trade-off between T_p and ϕ_{Hz} , the opposite sense to that seen for Hawaii (Figure 9e and h). While increasing the value of ϕ_{Hz} reduces the temperature drop during melting, it also decreases the total melt fraction. The inversion for Iceland is constrained particularly tightly by the requirement to produce a 20 km thick crust, any increase in ϕ_{Hz} must be compensated by an increase in T_p to maintain a sufficiently high total melt fraction.

834

835

836

837

838

839

840

841

842

843

844

845

846

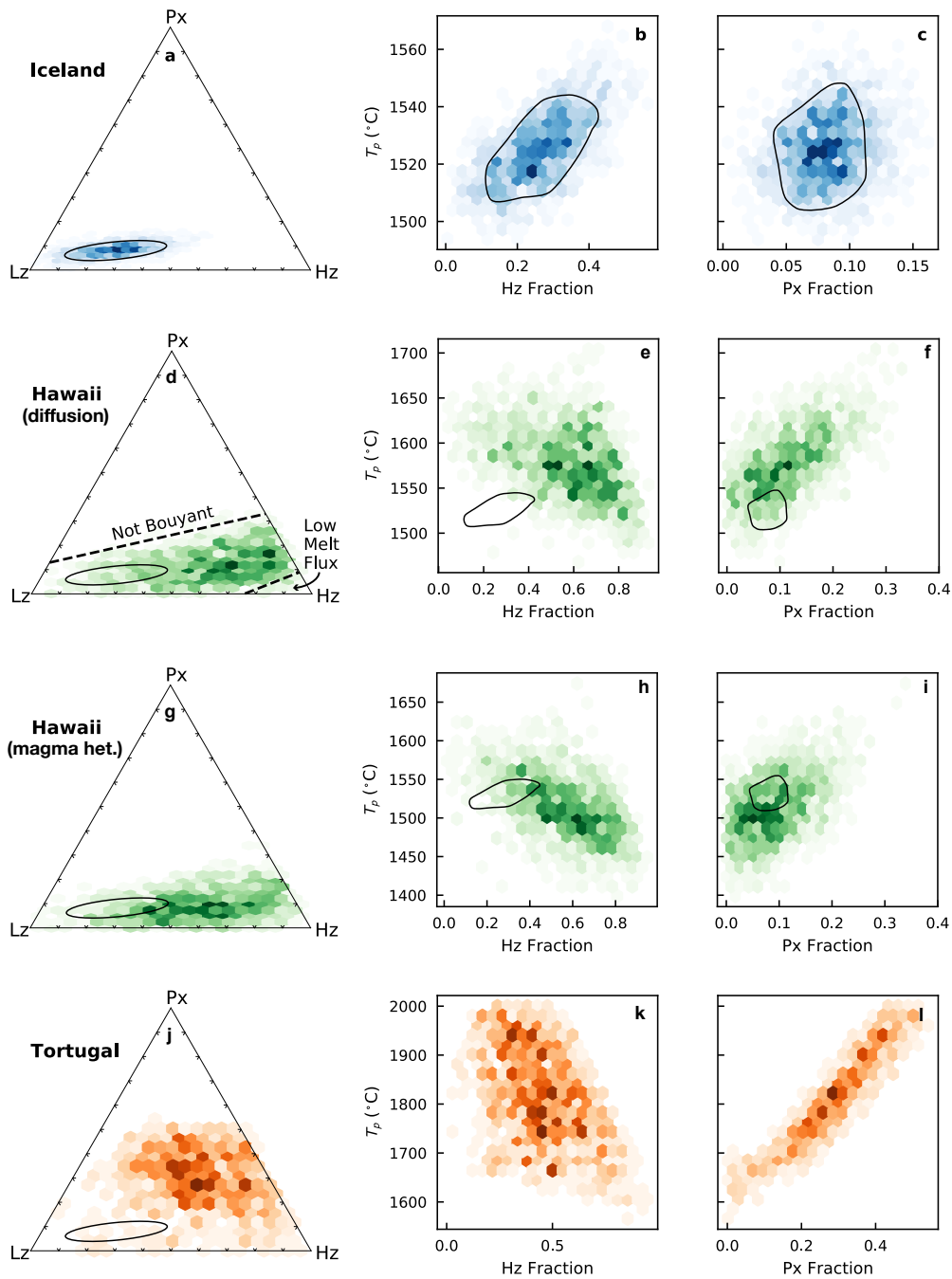
847

848

849

850

For a full discussion of how our T_p , ϕ_{px} , and ϕ_{Hz} estimates for Iceland compare to previous studies, the reader is referred to Matthews et al. (2016). A recent study by Brown et al. (2020a) takes a similar approach to estimating T_p and ϕ_{px} as applied here, albeit without matching a $T_{\text{crys}}^{\text{primary}}$ constraint. Rather than matching an imposed value of the relative proportion of pyroxenite- and lherzolite-derived melts, X_{px} , as we do (following Matthews et al., 2016; Shorttle et al., 2014), they match the full suite of trace element concentrations directly. Brown et al. (2020a) find no requirement for a harzburgite component in the source, which is discussed further by Shorttle et al. (2020) and Brown et al. (2020b). As shown in Figure 10 of Matthews et al. (2016), a significant harzburgite fraction is required in the mantle source even in the absence of an X_{px} constraint. As in the models by Matthews et al. (2016), we require a significant harzburgite fraction to simultaneously match crustal thickness and crystallization temperature. Since the Brown et al. (2020a) model does not attempt to match $T_{\text{crys}}^{\text{primary}}$, they do not require a harzburgite fraction. Our inversions suggest T_p is slightly higher than the inversions by Brown et al. (2020a), though we find a similar ΔT_p (relative to MORB). The difference between our (absolute) T_p estimate and the T_p estimate by Brown et al. (2020a) is due, in part, to the trade-off we see between T_p and ϕ_{Hz} (Figure 9b), and partly due to differences in the fusibility of our lherzolite melting



821 **Figure 9.** Posterior distributions for Iceland (a-c), Hawaii (d-i) and Tortugal (j-l) for mantle
 822 T_p , ϕ_{px} , and ϕ_{hz} . For Hawaii, results are shown for inversions using $T_{cryst}^{primary}$ estimates derived
 823 from both the diffusion correction and magma-heterogeneity correction methods. The annotations
 824 in panel a show the regions of parameter space in which solutions are prevented, on the basis of
 825 not producing a buoyant mantle plume, or being unable to match the observed magma flux. The
 826 shading shows the probability density. The black outline on plots a-i shows the approximate region
 827 of highest probability density for Iceland.

851 models. However, our estimate of ϕ_{px} ($8\pm 3\%$) is comparable to the 6.5-8.5% estimated by
 852 Brown et al. (2020a).

853 7.3 Hawaii

854 Here we summarise the results of the inversions for Hawaii, consider the effects each
 855 constraint has on the estimated T_p , and compare our T_p estimates to previous T_p estimates
 856 made for Hawaii.

857 7.3.1 The effects of different choices of $T_{\text{crys}}^{\text{primary}}$

858 In Figure 7 we show the posterior mantle T_p distributions for Hawaii, calculated using
 859 values of $T_{\text{crys}}^{\text{primary}}$ estimated with both the diffusive and magma-heterogeneity correction
 860 methods. The lower of the two mantle T_p estimates is based on the magma-heterogeneity
 861 correction, and falls close to the T_p we estimate for Iceland. The higher mantle T_p estimate
 862 is derived from the diffusive correction, but still overlaps with the Iceland posterior mantle
 863 T_p distribution. Both estimates demonstrate a robust elevation in Hawaiian T_p relative to
 864 Siqueiros (MORB).

865 Whilst the assumptions we make in obtaining a value for $T_{\text{crys}}^{\text{primary}}$ clearly have a large
 866 impact on the estimated mantle T_p , applying no correction to T_{crys} significantly decreases the
 867 estimated T_p to being not far in excess of Siqueiros (Figure 10). Such a small temperature
 868 excess over ambient mantle is in clear contradiction of other observations that are not
 869 formally included in the inversion (e.g., Watson & McKenzie, 1991; Watson, 1993), further
 870 reinforcing that comparison of T_{crys} is best made between the most primitive olivine crystals.

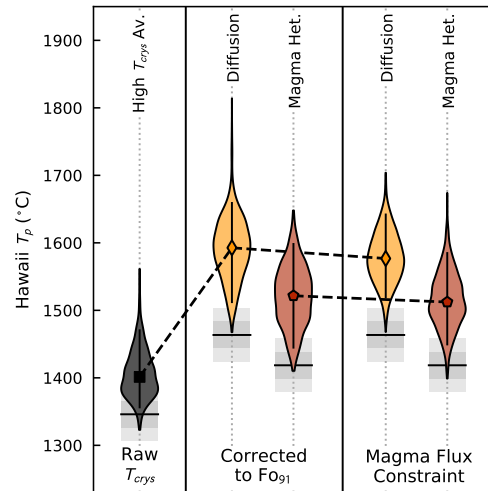
880 7.3.2 Effect of applying the Q_m constraint

881 Figure 10 shows the small effect that imposing the Q_m constraint (Wessel, 2016) has
 882 on the posterior mantle T_p distributions. Requiring the models to produce a sufficient melt
 883 flux prevents solutions with the most extreme ϕ_{hz} (Figure 9d). Since the solutions with the
 884 largest ϕ_{hz} produce the smallest correction for the latent heat of melting (Matthews et al.,
 885 2016), the lowest T_p solutions are no longer viable (Figure 10). Q_m provides a much weaker
 886 constraint on the Hawaii mantle T_p than t_{crust} provides for Siqueiros and Iceland because
 887 we set a wide prior on the plume conduit radius (Section 5).

888 7.3.3 Posterior constraints on ϕ_{px} and ϕ_{hz}

889 Unlike the inversions for Siqueiros and Iceland, little constraint is placed on ϕ_{px} and
 890 ϕ_{hz} for Hawaii. On the basis of olivine Ni contents A. V. Sobolev et al. (2005) suggested
 891 the Hawaiian mantle is olivine-free; however, further experimental work has cast doubt on
 892 this conclusion (Wang & Gaetani, 2008; Niu et al., 2011; Matzen et al., 2017). Though
 893 none of the lithologies used in our inversion are truly olivine free, the KG1 pyroxenite has
 894 a comparatively low modal abundance of olivine. Even when we use the KG1 model for
 895 the pyroxenitic lithology (which is less dense than an olivine-free pyroxenite, Shorttle et al.,
 896 2014), our results demonstrate that a $\phi_{\text{px}} = 100\%$ mantle is not simultaneously buoyant
 897 and compatible with our T_{crys} observations. Better constraints could be placed on ϕ_{px} and
 898 ϕ_{hz} with a more sophisticated model for forward modelling magma-flux, and the relative
 899 contributions of lherzolite- and pyroxenite-derived melts to it (X_{px} at ocean islands is likely
 900 to be particularly sensitive to the vertical gradient in mantle velocity field).

901 The posterior distributions from the inversions using both estimates of $T_{\text{crys}}^{\text{primary}}$ demon-
 902 strate a negative trade-off between T_p and ϕ_{hz} . The higher the mantle ϕ_{hz} , the greater the
 903 thermal buffering effect and, therefore, the smaller the temperature drop during melting.
 904 In the inversion where we match the diffusion-corrected $T_{\text{crys}}^{\text{primary}}$, a positive trade-off is ob-



871 **Figure 10.** Effect on the posterior Hawaii mantle T_p distribution of the various treatments of
 872 the raw observations discussed in the text. The left-most distribution is calculated by treating the
 873 raw crystallization temperatures (T_{crys}) as primary crystallization temperatures (Figure 5a). The
 874 middle distributions are calculated from the inferred T_{crys} for Fo_{91} olivine crystals, assuming that
 875 either the scatter in the raw T_{crys} population represents diffusion, as shown in Figure 5b, or arises
 876 from magma heterogeneity, demonstrated in Figure 5c. The right-most distributions are generated
 877 from the same T_{crys} inferred for Fo_{91} crystals, but the inversions were also required to match the
 878 magma flux constraint. The horizontal bars show the values of T_{crys} used in each inversion, with
 879 their one and two s.d. uncertainties indicated by shading.

served with ϕ_{px} . Increasing mantle ϕ_{px} causes both the mantle density and the temperature drop during melting to increase; both effects are offset by a higher mantle T_p .

Figure 9 shows the circumstances in which the Hawaiian $T_{\text{crys}}^{\text{primary}}$ and Q_m values are consistent with Hawaii having the same mantle T_p as Iceland. For the higher T_p solution, the most harzburgitic solutions for Hawaii have a similar T_p to the solutions for Iceland (black outline on Figure 9e). In this case, a single mantle T_p may satisfy both the Iceland and Hawaii constraints, if there is significant ϕ_{hz} variability in the mantle. For the lower T_p solution, derived from the magma-heterogeneity correction, the highest T_p solutions for Iceland overlap with the posterior Hawaii distributions in both T_p and $\phi_{\text{px}}-\phi_{\text{hz}}$ space (Figure 9h and i). If the magma-heterogeneity correction is the most appropriate method for estimating $T_{\text{crys}}^{\text{primary}}$, the same mantle T_p , ϕ_{px} , and ϕ_{hz} can account for both Hawaii and Iceland, despite their differing T_{crys} values.

Recent plume buoyancy flux estimates (Hoggard et al., 2020; Ribe et al., 2020) suggest the strength of plume upwelling beneath Hawaii is either less strong, or similarly strong to plume upwelling beneath Iceland. Neglecting variation in plume conduit radius, this might be taken to suggest solutions for Hawaii with lower plume buoyancy, i.e. lower T_p , higher ϕ_{px} , and lower ϕ_{hz} , are the most likely. This might, in turn, be taken to suggest the magma-heterogeneity correction is the most appropriate method for estimating $T_{\text{crys}}^{\text{primary}}$, as using this T_{crys} in the inversion results in a greater number of viable solutions that have lower buoyancy than the solutions for Iceland.

7.3.4 Comparison to previous T_p estimates

Our highest mantle T_p estimate for Hawaii (1582^{+68}_{-65} °C) is within uncertainty of the T_p value (1630 ± 77 °C) estimated by Putirka et al. (2018), also derived from an estimate of $T_{\text{crys}}^{\text{primary}}$. However, our estimate for $T_{\text{crys}}^{\text{primary}}$ itself (1464 ± 20 °C) is much lower than the 1549 °C estimated by Putirka et al. (2018); this discrepancy likely arises from, either, our correction routine underestimating $T_{\text{crys}}^{\text{primary}}$, or the olivine and melt compositions used by Putirka et al. (2018) never having been in equilibrium, as suggested elsewhere (Herzberg, 2011; Matthews et al., 2016; Hole & Natland, 2019). The larger latent heat of melting correction from which our median T_p is calculated reflects the slightly higher median total melt fraction than estimated by Putirka et al. (2018), though the estimates are within uncertainty.

The T_p of 1526 °C estimated for Hawaii by Herzberg and Asimow (2015) using the PRIMELT3 algorithm is intermediate (and within error of) both of our T_p estimates, but is closer to our lower estimate, derived using the magma heterogeneity correction routine. Since Herzberg and Asimow (2015) implicitly assume that lithological heterogeneity has a negligible effect on the melting region geotherm, the coincidence of our T_p estimates indicates the effects of harzburgite and pyroxenite approximately cancel each other out for our mid-range T_p solutions.

Using REE-inversions White and M^cKenzie (1995) estimated a T_p for Hawaii of ~ 1450 °C, lower than their T_p estimate for Iceland, and only consistent (within uncertainty) with the lower of our two T_p estimates. Compared to our model, we might expect REE-inversions to systematically over-estimate T_p , as any harzburgite present will elevate melt fractions at any given depth, the primary discriminator for T_p the White and M^cKenzie (1995) model is sensitive to (Appendix A). However, the opposite effect is seen, and might reflect the mantle REE-concentrations being too low in their inversion.

7.4 The North Atlantic Igneous Province

In our inversions, all of the North Atlantic Igneous Province (NAIP) locations have estimated T_p values within uncertainty of our estimate for modern Iceland. The median T_p estimates for Rum and Skye fall only slightly higher than the median Iceland T_p , despite

954 their T_{cryst} estimates being far in excess of those for Iceland (Spice et al., 2016). The higher
 955 T_{cryst} values, in absence of a significant difference in T_p , are mostly accounted for by the
 956 smaller latent heat of melting correction resulting from the presence of thick lithosphere
 957 beneath Rum and Skye. In contrast, the modest elevation in T_{cryst} for Mull, Baffin, SE
 958 Greenland and W Greenland, is not sufficiently offset by the presence of thick lithosphere,
 959 meaning that the median T_p estimates for the mantle sampled by these eruptions falls lower
 960 than the mantle T_p estimate for modern Iceland. Here we discuss how our new T_p estimates
 961 relate to previously published estimates, for a more thorough discussion of how previous T_p
 962 estimates within the NAIP compare with each other, see Hole and Natland (2019).

963 Using a combination of geochemistry, geophysics and T_{cryst} observations, Spice et al.
 964 (2016) inferred temporal variation in the T_p of the Iceland plume; the hottest temperatures at
 965 the time of impact and the coolest temperatures in the Tertiary. Whilst the tertiary Iceland
 966 olivines have lower T_{cryst} than the recent Iceland and NAIP olivines, they are less forsteritic,
 967 implying a greater degree of magmatic evolution. We apply our correction methods to this
 968 dataset and estimate a $T_{\text{cryst}}^{\text{primary}}$ of 1423°C using the diffusive correction, and 1347°C using
 969 the magma heterogeneity correction (Supporting Figure S.3). Once the correction has been
 970 applied, the Tertiary Iceland $T_{\text{cryst}}^{\text{primary}}$ could be either greater or lower than modern-day
 971 Iceland, and comparable to or slightly lower than the NAIP. As the tectonic setting of the
 972 Tertiary lava sequence in Iceland is somewhat uncertain, we do not formally invert the
 973 $T_{\text{cryst}}^{\text{primary}}$ estimates. However, it seems likely that the magnitude of the correction needed to
 974 go from T_{cryst} to T_p should be intermediate between Iceland and the NAIP lavas, suggesting
 975 T_p during the Tertiary is likely in the range 1400–1570°C. Our results, therefore, suggest
 976 that T_{cryst} observations from the NAIP, Tertiary Iceland, and modern Iceland, do not provide
 977 supporting evidence for the temporal T_p change suggested by Spice et al. (2016), based on
 978 geochemical and geophysical observations.

979 Putirka et al. (2018) estimate the mantle T_p for Baffin as $1630 \pm 65^\circ\text{C}$, higher than,
 980 but within mutual uncertainty of, our estimate. Our median estimates of T_p differ for
 981 two reasons. First, Putirka et al. (2018) estimate a higher melt-olivine (Fo_{92}) equilibration
 982 temperature (1512°C) than the olivine-spinel equilibration temperatures recorded by the
 983 most forsteritic olivine crystals (Spice et al., 2016), the average of which ($1413 \pm 22^\circ\text{C}$) we
 984 use in our inversion. Second, Putirka et al. (2018) estimate a slightly higher bulk melt
 985 fraction (0.239 ± 41) than our median result (~ 0.15 , Supporting Table S.5). Interestingly,
 986 our estimated melt fraction for the lherzolite component (~ 0.23 , Supporting Table S.5) is
 987 very similar to the estimate by Putirka et al. (2018), who assumed a purely lherzolitic source.
 988 The discrepancy in our estimates of crystallization temperature might reflect the olivine-
 989 spinel thermometer missing some crystallization history, hidden perhaps by re-equilibration
 990 of olivine Fo contents with more primitive melts. Alternatively, the olivine-melt thermometer
 991 may be in error if an incorrect melt composition was chosen (Herzberg, 2011; Matthews et
 992 al., 2016; Hole & Natland, 2019).

993 REE-inversions performed on a number of NAIP lavas (White & M^cKenzie, 1995)
 994 suggest that the mantle T_p was not significantly different from the present-day Iceland T_p
 995 of $\sim 1500^\circ\text{C}$, consistent with our results. Whilst the presence of harzburgite might bias the
 996 REE-inversions towards high values of T_p , the presence of trace-element enriched pyroxenite
 997 will tend to bias the inversions towards lower T_p values. It is possible that the effects of
 998 pyroxenite and harzburgite act to offset each other, bringing our T_p estimates into line with
 999 those of White and M^cKenzie (1995). Though we incorporate pyroxenite and harzburgite
 1000 into our T_p inversions, in our median T_p solutions their effects may also cancel out.

1001 Hole and Millett (2016) applied the PRIMELT3 algorithm to a large number of sam-
 1002 ples from the NAIP, finding evidence for a T_p of $\sim 1550^\circ\text{C}$ for Baffin Island and Disko
 1003 Island, and a T_p of $1500\text{--}1510^\circ\text{C}$ for the British portions of the NAIP and present-day Ice-
 1004 land. Whilst we don't see the offset between Baffin and the other NAIP localities, the T_p
 1005 values estimated by Hole and Millett (2016) are within uncertainty of our own. Applying
 1006 PRIMELT3 to lavas from Baffin and West Greenland, Willhite et al. (2019) find a T_p value

1007 of 1510-1630°C, overlapping with our T_p estimates, but extending to much higher values.
 1008 This discrepancy could reflect either the presence of harzburgite in the source, leading to
 1009 PRIMELT3 overestimating T_p , or to magmas losing heat as they transit the lithosphere,
 1010 yielding low values of T_{crys} .

1011 7.5 The Caribbean Large Igneous Province

1012 More extreme variations in median T_p are seen for the Caribbean LIP (Figure 7).
 1013 Whilst Curaçao and Gorgona exhibit overlapping posterior T_p distributions, the posterior
 1014 distribution for Tortugal is significantly higher and represents the highest T_p calculated here.
 1015 The mantle T_p calculated for Gorgona is within uncertainty of our estimate for Iceland,
 1016 whilst the Curaçao T_p is within uncertainty of MORB. This low value of mantle T_p for
 1017 Curaçao might reflect an insufficient correction for crystallization in calculating the Curaçao
 1018 $T_{\text{crys}}^{\text{primary}}$.

1019 In the inversions we set the same prior for lithospheric thickness (60 ± 10 km) on all
 1020 three locations. The apparent shift in T_p may, therefore, instead reflect variable lithospheric
 1021 thickness in the vicinity of a spreading centre, as suggested by Trela et al. (2017). In addition
 1022 to variable lithospheric thickness, Trela et al. (2017) argue that the T_{crys} observations require
 1023 variable mantle T_p .

1024 Our mantle T_p estimates are considerably lower ($\sim 180^\circ\text{C}$ for Curaçao and Gorgona)
 1025 than those Trela et al. (2017) calculated from whole rock major element chemistry using
 1026 PRIMELT3. Whilst an underestimation of the required correction to the Curaçao T_{crys} to
 1027 estimate $T_{\text{crys}}^{\text{primary}}$ might seem an appealing solution to the discrepancy, we apply no such
 1028 correction to Gorgona, obtaining $T_{\text{crys}}^{\text{primary}}$ directly from extremely forsteritic crystals. As
 1029 for the discrepancy in NAIP results discussed in the preceding section, the discrepancy here
 1030 might also arise from significant harzburgite in the mantle source, or heat loss during magma
 1031 transport.

1032 Trela et al. (2017) estimate the mantle T_p for Tortugal as $\sim 1800^\circ\text{C}$, very close to
 1033 our estimate of 1813_{-149}^{+157} °C. The T_{crys} observations are, therefore, consistent with the T_p
 1034 estimate by Trela et al. (2017) when the relationship between mantle T_p and $T_{\text{crys}}^{\text{primary}}$ is
 1035 robustly quantified. However, whilst the median T_p estimate for Tortugal is significantly
 1036 higher than for the other locations, it is within uncertainty of Emeishan, Karoo, Etendeka
 1037 and Hawaii. Figure 9k and 9l demonstrate that the very high Tortugal $T_{\text{crys}}^{\text{primary}}$ can be
 1038 matched with a more moderate mantle T_p if ϕ_{hz} is high and ϕ_{px} is low. This possibility
 1039 contrasts with the interpretations of Trela et al. (2017), who suggested the Tortugal magmas
 1040 were derived from an extremely hot mantle plume, akin to Archean plumes that gave rise
 1041 to komatiites (e.g., Nisbet et al., 1993).

1042 Whilst explaining both Archean komatiites and the Tortugal Phanerozoic komatiite
 1043 with the same mechanism is appealing, it is difficult to reconcile the existence of a uniquely
 1044 hot mantle plume in the Phanerozoic with the intrinsic dynamical instability of hot mantle
 1045 material and the rapidity of thermal diffusion (Shorttle, 2017). The trade-off between mantle
 1046 T_p and ϕ_{px} (Figure 9) demonstrates the plume could have been anomalously pyroxenite rich,
 1047 perhaps making the bulk material anomalously dense and, therefore, requiring significant
 1048 heating before a convective instability developed. We propose an alternative mechanism,
 1049 corresponding to the lower T_p region of the posterior distribution, whereby the mantle
 1050 giving rise to the Tortugal komatiite was anomalously harzburgite-rich and contained a small
 1051 volume-fraction of more fusible material. The harzburgite would then buffer the temperature
 1052 during melting to produce extremely hot, high melt-fraction, melts of the fusible material,
 1053 despite having a T_p similar to that of other Phanerozoic mantle plumes.

1054

7.6 Karoo, Emeishan and Etendeka Large Igneous Provinces

1055

1056

1057

1058

1059

1060

The mantle T_p estimates for the Karoo, Emeishan and Etendeka LIPs are the most uncertain of all the T_p estimates presented here. The large uncertainty derives from high crystallization temperatures favouring high T_p solutions: higher mantle T_p enables higher ϕ_{px} before the mantle loses its buoyancy, thereby enlarging the range of lithology space of viable solutions. All three LIP mantle T_p estimates are within uncertainty of the mantle T_p for both Iceland and Hawaii (Figure 7).

1061

1062

1063

1064

1065

1066

1067

1068

1069

1070

1071

1072

Our estimate of the T_p for the Emeishan LIP (1555^{+100}_{-97} °C) corresponds well with the previous T_p estimates (1560–1600°C) made by Ali et al. (2010) and He et al. (2010) using the PRIMELT2 algorithm (Herzberg & Asimow, 2008). Tao et al. (2015) estimated a T_p of 1740–1810°C using the same methodology as Putirka (2008a), much higher and outside the uncertainty of our value. The high T_p estimate derives from the high value of $T_{\text{crys}}^{\text{primary}}$ (up to 1536°C) estimated by Tao et al. (2015). If there is significant heterogeneity in magma composition during crystallization of the most forsteritic olivines, an incorrect choice of primary magma chemistry for use in the olivine-liquid thermometer might result in an overestimate of $T_{\text{crys}}^{\text{primary}}$ (Herzberg, 2011; Matthews et al., 2016). Putirka et al. (2018) estimate an even higher $T_{\text{crys}}^{\text{primary}}$ for Emeishan, of 1597°C; however, their lower estimate of the total melt fraction gave a slightly lower T_p estimate of 1700 ± 67 °C than Tao et al. (2015).

1073

1074

1075

1076

1077

1078

1079

1080

1081

1082

1083

1084

1085

1086

1087

In estimating the T_p for the Karoo LIP we use the T_{crys} observations by Heinonen et al. (2015), who also estimated mantle T_p from T_{crys} . To estimate the latent heat of melting correction Heinonen et al. (2015) applied the Putirka et al. (2007) parameterizations for the relationship between lava major element chemistry and melt fraction, and, therefore, the magnitude of the latent heat of melting. They estimated T_p in the range 1540–1640°C, within uncertainty of our own estimate (1601^{+193}_{-103}). Heinonen et al. (2015) also applied PRIMELT3 (Herzberg & Asimow, 2015) to the lava major element chemistry, yielding a T_p of 1630°C. Despite not including the role of lithological heterogeneity, these estimates coincide with our own, suggesting that in our median solution the effects of harzburgite and pyroxenite cancel out. A higher T_p estimate of 1785 ± 55 °C was made by Putirka (2016), though it is still within uncertainty of our estimate. White (1997) used REE-inversions to estimate the T_p for Karoo, finding a much lower value of ~ 1450 °C. Observations of ~ 1450 °C crystallization temperatures suggest that the REE-inversions are significantly underestimating T_p , most likely due to an inappropriate choice of mantle source REE concentrations, or neglect of the effects of plume-driven upwelling (MacLennan et al., 2001).

1088

1089

1090

1091

1092

1093

1094

1095

Our T_p estimate for Etendeka (1599^{+104}_{-79} °C) agrees well with the T_p estimate made by Jennings et al. (2019) (1623^{+22}_{-20} °C) using the same T_{crys} observations and a similar methodology for the latent heat of melting correction. Jennings et al. (2019) produce a much more precise estimate since they do not consider lithological heterogeneity. Once again, the near-coincidence of our median T_p estimate indicates that in our median solution the effects of harzburgite and pyroxenite cancel each other out. Both estimates are also within uncertainty of the Putirka (2016) T_p estimate of 1596 ± 43 , though like the localities previously discussed, this T_p estimate is derived from a higher value of $T_{\text{crys}}^{\text{primary}}$ (1515°C).

1096

8 Summary

1097

1098

1099

1100

1101

1102

1103

Petrological techniques for estimating mantle T_p allow us to assess T_p on the ancient Earth, where we do not always have reliable constraints from seismic tomography, magma productivity estimates and geomorphology. Previous studies employing the olivine-spinel Al-exchange thermometer have inferred high mantle T_p during the generation of large igneous provinces on the basis on the higher crystallization temperatures their olivine cargoes record. In this paper we have laid out a methodology for quantitatively assessing the constraints crystallization temperatures place on mantle T_p , accounting for potential bi-

ases in the crystallization temperature record introduced by lithological heterogeneity and lithosphere thickness. This is an important step in validating the use of crystallization temperature estimates for inferring variability in mantle T_p .

In our inverted dataset we have two locations of modern-day mantle-plume volcanism: Hawaii and Iceland. As discussed in Section 7.3, the inverted T_p for Hawaii is much more uncertain than for Iceland; we show that our new crystallization temperature estimates and the previously estimated magma flux for Hawaii are consistent with mantle T_p both similar and in excess of Iceland, depending on how the raw crystallization temperature observations are treated (Figure 7). The uncertainty on the T_p estimates for the Emeishan, Karoo, and Etendeka large igneous provinces also places them just within uncertainty of the Iceland T_p . All of the NAIP localities have inverted mantle T_p well within uncertainty of the present-day Iceland T_p .

The Tortugal komatiite olivine crystallization temperatures are consistent with a very hot mantle plume, as suggested by Trela et al. (2017), but are also consistent with a plume temperature similar to that of the Emeishan, Karoo, and Etendeka LIPs, in addition to the highest T_p solutions for Hawaii. Such anomalously hot magmas may be derived from a mantle composed largely of harzburgite with a small volume fraction of more fusible mantle components (Figure 9k). If we assume that the mantle T_p for Tortugal is similar to the T_p for Hawaii and LIPs, all of these locations must have mantle T_p in excess of Iceland.

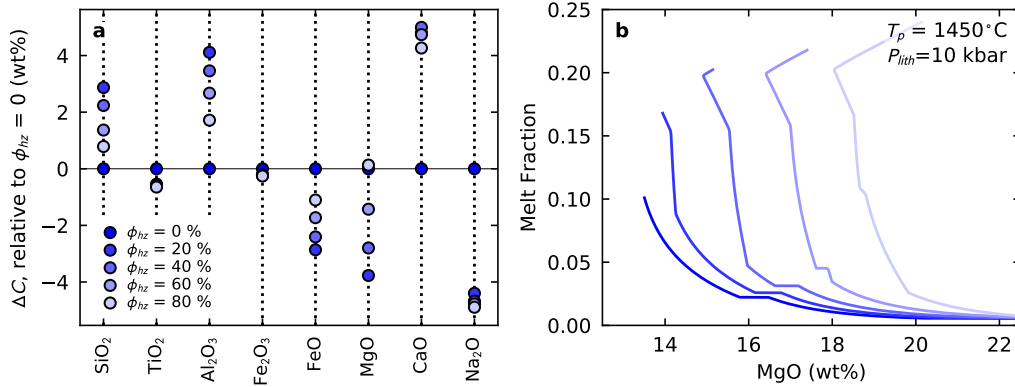
In summary, all of the plume localities we consider here, with the exception of Curaçao, require a mantle temperature significantly in excess of ambient mantle to explain their high crystallization temperatures. The uncertainty introduced from variable mantle lithology means it is generally impossible to infer differences in mantle T_p between mantle plumes from crystallization temperatures alone. However, it is likely that at least two values of mantle plume T_p are required to explain the crystallization temperatures of Phanerozoic plume-derived magmas.

A The effect of harzburgite on melt chemistry

When significant quantities of harzburgite are present in the melting region it can act as a thermal buffer, providing heat to the lithologies undergoing melting. This extra heat energy is partly consumed by the melting reactions, enhancing melt production, but also allows the mantle to retain higher temperatures at any given pressure relative to a harzburgite-free mantle (Shorttle et al., 2014; Matthews et al., 2016). Consequently, for a given T_p , a harzburgite-rich mantle will see higher melting temperatures, which will, in turn, affect the major- and trace-element chemistry of its derivative melts.

To demonstrate this effect we used the alphaMELTS software (Smith & Asimow, 2005) running the pMELTS model (Ghiorso et al., 2002) to predict the major- and trace-element compositions of melts produced during continuous adiabatic decompression melting, with a porosity of 0.5%. To incorporate the effects of lithological heterogeneity, we used our multi-lithologic melting model (described in the main text) to calculate the pressure-temperature path followed by the mantle with $\phi_{\text{hz}} = 0, 0.2, 0.4, 0.6, \text{ and } 0.8$, at a T_p of 1450°C. We did not include any pyroxenite component in the models.

We then ran alphaMELTS along this prescribed pressure-temperature path, starting at 3.95 GPa, and ending at 1 GPa. The initial bulk-composition was set to the depleted mantle of Workman and Hart (2005), in the NCFMASTO system. The partition coefficients for the trace-elements were set to their default values (M^cKenzie & O’Nions, 1991, 1995). To obtain aggregate melts, the extracted melt compositions were summed with equal weighting, up to the pressure at the base of the lithosphere (either 10 or 16 kbar). Due to the discrepancy in solidus position between pMELTS and our parameterization for KLB-1 lherzolite, all the alphaMELTS calculations started just above the solidus, generating a small quantity of very low-fraction melts.

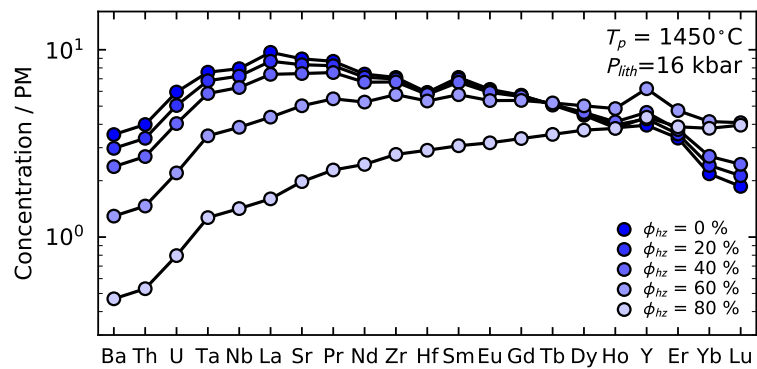


1154 **Figure A.1.** Results from pMELTS calculations of adiabatic decompression melting of mantle
 1155 with a T_p of $1450^\circ C$, and varying proportions of lherzolite and harzburgite (ϕ_{hz}). Melting was
 1156 terminated at 10 kbar. See text for more information on how the calculations were performed.
 1157 Panel a shows the effect of increasing ϕ_{hz} on the major-element composition of aggregate melts.
 1158 Panel b shows how melt MgO varies with melt fraction for each of the models, the color and shading of
 1159 the lines matches the key in panel a. The tail of high MgO at low melt fraction is an artefact of
 1160 the calculation method.

1161 Figure A.1 demonstrates that the major-element compositions of lherzolite-derived
 1162 melts is sensitive to the fraction of harzburgite in the source, causing a change of over
 1163 4 wt% for some oxides in the aggregate melts. Of particular relevance for estimating mantle
 1164 T_p is the control of harzburgite fraction of the MgO content of melts. For example, the MgO
 1165 content of primary melts is a key parameter in the PRIMELT algorithms for determining
 1166 T_p (Herzberg & Asimow, 2008, 2015). Figure A.1b demonstrates that while MgO stays
 1167 approximately constant for most of the adiabatic decompression path, the near-constant
 1168 MgO value is dependent on ϕ_{hz} . High melt MgO could, therefore, be a product of both high
 1169 mantle T_p and high ϕ_{hz} . In particular, the absence of high melt fluxes despite the presence
 1170 of high MgO lavas, might be indicative of a largely harzburgitic mantle, rather than extreme
 1171 values of mantle T_p .

1179 Since the presence of harzburgite in the melting region can significantly increase the
 1180 melt fraction of coexisting lherzolite, the phase assemblage equilibrating with the liquid
 1181 will also be a function of ϕ_{hz} . This, in turn, will affect the trace-element chemistry of the
 1182 derivative melts, demonstrated in Figure A.2. The pressure at the base of the lithosphere
 1183 was set to 16 kbar in these calculations, such that the $\phi_{hz} = 0$ case has a pronounced “garnet-
 1184 signature” in its aggregate melts; i.e. a downward trend in normalised concentration is seen
 1185 in the heavy rare-earth elements at the right-hand side of Figure A.2.

1186 As the fraction of harzburgite in the mantle increases, the garnet signature in the
 1187 aggregate melts is progressively lost, the concentrations of all trace-elements becomes in-
 1188 creasingly diluted, and the signal of extremely incompatible-element depletion (left-hand
 1189 side of Figure A.2) becomes stronger. These changes in the trace-element systematics are
 1190 all the result of increased lherzolite melt fraction. This is of relevance for T_p estimation as
 1191 REE-inversions (McKenzie & O’Nions, 1991) use these systematics to identify mantle T_p .
 1192 However, we have demonstrated that harzburgite fraction – independent of mantle T_p – can
 1193 substantially change the trace-element systematics of lavas. This further demonstrates the
 1194 power of combining geochemical observations with geophysical constraints on magma flux,
 1195 to simultaneously identify mantle T_p , ϕ_{px} , and ϕ_{hz} .



1172 **Figure A.2.** The aggregate melt trace-element chemistry calculated by alphaMELTS (imple-
 1173 menting pMELTS) for adiabatic decompression melting of mantle with a T_p of 1450°C , and varying
 1174 proportions of lherzolite and harzburgite (ϕ_{hz}). The trace element chemistry of the solid lherzolite
 1175 was set to the Average DMM of Workman and Hart (2005), the harzburgite did not contribute to
 1176 the melts. Melting was terminated at 16 kbar. See text for more information on how the calculations
 1177 were performed. Concentrations are normalized to the primitive mantle composition of Palme and
 1178 O'Neill (2014).

1196 **Acknowledgments**

1197 The authors would like to thank Michael Perfit for provision of the Siqueiros samples and
 1198 for his comments on a draft of the manuscript. Iris Buisman and Carrie Soderman are
 1199 thanked for their help with the electron probe analyses. Claude Herzberg, Keith Putirka,
 1200 Godfrey Fitton, and one anonymous reviewer are thanked for their constructive feedback
 1201 and efforts to improve the manuscript. The figures in this publication were produced using
 1202 the Matplotlib python library (Hunter, 2007). This work was supported by a Natural
 1203 Environment Research Council studentship [NE/L002507/1 and NE/M000427/1] to SM.
 1204 The analytical data generated by this study is provided in the Supporting Data Sets S.2.
 1205 and S.4. The python module used to perform the mantle melting calculations (pyMelt) is
 1206 archived in a Zenodo repository (Matthews et al., 2020). The extension for performing the
 1207 Bayesian inversion calculations (pyMelt_multinest) is also archived in a Zenodo repository
 1208 (Matthews & Shorttle, 2020).

1209 **References**

- 1210 Aghaei, O., Nedimović, M. R., Carton, H., Carbotte, S. M., Canales, J. P., & Mutter,
 1211 J. C. (2014). Crustal thickness and moho character of the fast-spreading East Pacific
 1212 rise from 9° 42'N to 9° 57'N from poststack-migrated 3-D MCS data. *Geochemistry,
 1213 Geophysics, Geosystems*, 15(3), 634–657.
- 1214 Ali, J. R., Fitton, J. G., & Herzberg, C. (2010). Emeishan large igneous province (SW
 1215 China) and the mantle-plume up-doming hypothesis. *Journal of the Geological Society*,
 1216 167(5), 953–959.
- 1217 Alvarado, G. E., Denyer, P., & Sinton, C. W. (1997). The 89 Ma Tortugal komatiitic suite,
 1218 Costa Rica: implications for a common geological origin of the Caribbean and Eastern
 1219 Pacific region from a mantle plume. *Geology*, 25(5), 439–442.
- 1220 Bizimis, M., Griselin, M., Lassiter, J. C., Salters, V. J., & Sen, G. (2007). Ancient recycled
 1221 mantle lithosphere in the Hawaiian plume: osmium–hafnium isotopic evidence from
 1222 peridotite mantle xenoliths. *Earth and Planetary Science Letters*, 257(1), 259–273.
- 1223 Bock, G. (1991). Long-period S to P converted waves and the onset of partial melting
 1224 beneath Oahu, Hawaii. *Geophysical Research Letters*, 18(5), 869–872.
- 1225 Boudier, F., & Coleman, R. (1981). Cross section through the peridotite in the Samail
 1226 ophiolite, southeastern Oman Mountains. *Journal of Geophysical Research: Solid
 1227 Earth*, 86(B4), 2573–2592.
- 1228 Bown, J. W., & White, R. S. (1994). Variation with spreading rate of oceanic crustal
 1229 thickness and geochemistry. *Earth and Planetary Science Letters*, 121(3-4), 435–449.
- 1230 Brown, E. L., Petersen, K. D., & Leshner, C. E. (2020a). Markov chain Monte Carlo
 1231 inversion of mantle temperature and source composition, with application to Reykjanes
 1232 Peninsula, Iceland. *Earth and Planetary Science Letters*, 532, 116007.
- 1233 Brown, E. L., Petersen, K. D., & Leshner, C. E. (2020b). Reply to “finding harzburgite in
 1234 the mantle. a comment on brown et al.(2020):‘markov chain monte carlo inversion of
 1235 mantle temperature and source composition, with application to reykjanes peninsula,
 1236 iceland’” by shorttle et al.
- 1237 Buchner, J., Georgakakis, A., Nandra, K., Hsu, L., Rangel, C., Brightman, M., . . . Kocevski,
 1238 D. (2014). X-ray spectral modelling of the AGN obscuring region in the CDFS:
 1239 Bayesian model selection and catalogue. *Astronomy & Astrophysics*, 564, A125.
- 1240 Byerly, B. L., & Lassiter, J. C. (2014). Isotopically ultradepleted domains in the convecting
 1241 upper mantle: Implications for MORB petrogenesis. *Geology*, 42(3), 203–206.
- 1242 Campbell, I. H., Griffiths, R., & Hill, R. (1989). Melting in an Archaean mantle plume:
 1243 heads it’s basalts, tails it’s komatiites. *Nature*, 339(6227), 697.
- 1244 Campbell, I. H., & Griffiths, R. W. (1990). Implications of mantle plume structure for the
 1245 evolution of flood basalts. *Earth and Planetary Science Letters*, 99(1-2), 79–93.
- 1246 Cashman, K. V., Sparks, R. S. J., & Blundy, J. D. (2017). Vertically extensive and unstable
 1247 magmatic systems: a unified view of igneous processes. *Science*, 355(6331).

- 1248 Cawthorn, R. G. (1975). Degrees of melting in mantle diapirs and the origin of ultrabasic
1249 liquids. *Earth and Planetary Science Letters*, *27*(1), 113–120.
- 1250 Coogan, L., Saunders, A., & Wilson, R. (2014). Aluminum-in-olivine thermometry of
1251 primitive basalts: evidence of an anomalously hot mantle source for large igneous
1252 provinces. *Chemical Geology*, *368*, 1–10.
- 1253 Dannberg, J., & Sobolev, S. V. (2015). Low-buoyancy thermochemical plumes resolve
1254 controversy of classical mantle plume concept. *Nature communications*, *6*(1), 1–9.
- 1255 Darbyshire, F. A., Priestley, K. F., White, R. S., Stefánsson, R., Gudmundsson, G. B., &
1256 Jakobsdóttir, S. S. (2000). Crustal structure of central and northern Iceland from
1257 analysis of teleseismic receiver functions. *Geophysical Journal International*, *143*(1),
1258 163–184.
- 1259 Davis, M., White, N., Priestley, K., Baptie, B., & Tilmann, F. (2012). Crustal structure of
1260 the British Isles and its epeirogenic consequences. *Geophysical Journal International*,
1261 *190*(2), 705–725.
- 1262 Droop, G. (1987). A general equation for estimating Fe³⁺ concentrations in ferromagnesian
1263 silicates and oxides from microprobe analyses, using stoichiometric criteria. *Miner-
1264 ological magazine*, *51*(361), 431–435.
- 1265 D’Errico, M. E., Warren, J., & Godard, M. (2016). Evidence for chemically heterogeneous
1266 Arctic mantle beneath the Gakkel Ridge. *Geochimica et Cosmochimica Acta*, *174*,
1267 291–312.
- 1268 Eggins, S. (1992). Petrogenesis of Hawaiian tholeiites: 1, phase equilibria constraints.
1269 *Contributions to Mineralogy and Petrology*, *110*(2-3), 387–397.
- 1270 Falloon, T. J., Green, D. H., Danyushevsky, L. V., & Faul, U. H. (1999). Peridotite
1271 melting at 1.0 and 1.5 GPa: an experimental evaluation of techniques using diamond
1272 aggregates and mineral mixes for determination of near-solidus melts. *Journal of
1273 Petrology*, *40*(9), 1343–1375.
- 1274 Farnetani, D. G., & Richards, M. A. (1995). Thermal entrainment and melting in mantle
1275 plumes. *Earth and Planetary Science Letters*, *136*(3-4), 251–267.
- 1276 Feroz, F., & Hobson, M. (2008). Multimodal nested sampling: an efficient and robust
1277 alternative to Markov Chain Monte Carlo methods for astronomical data analyses.
1278 *Monthly Notices of the Royal Astronomical Society*, *384*(2), 449–463.
- 1279 Feroz, F., Hobson, M., & Bridges, M. (2009). Multinest: an efficient and robust bayesian
1280 inference tool for cosmology and particle physics. *Monthly Notices of the Royal As-
1281 tronomical Society*, *398*(4), 1601–1614.
- 1282 Feroz, F., Hobson, M., Cameron, E., & Pettitt, A. (2013). Importance nested sampling and
1283 the MultiNest algorithm. *arXiv preprint arXiv:1306.2144*.
- 1284 Geissler, W. H., Sodoudi, F., & Kind, R. (2010). Thickness of the central and eastern Eu-
1285 ropean lithosphere as seen by s receiver functions. *Geophysical Journal International*,
1286 *181*(2), 604–634.
- 1287 Ghiorso, M. S., Hirschmann, M. M., Reiners, P. W., & Kress III, V. C. (2002). The
1288 pMELTS: A revision of MELTS for improved calculation of phase relations and major
1289 element partitioning related to partial melting of the mantle to 3 GPa. *Geochemistry,
1290 Geophysics, Geosystems*, *3*(5), 1–35.
- 1291 Gill, R., Pedersen, A. K., & Larsen, J. (1992). Tertiary picrites in West Greenland: melting
1292 at the periphery of a plume? *Geological Society, London, Special Publications*, *68*(1),
1293 335–348.
- 1294 Gilligan, A., Bastow, I. D., & Darbyshire, F. A. (2016). Seismological structure of the 1.8
1295 Ga Trans-Hudson Orogen of North America. *Geochemistry, Geophysics, Geosystems*,
1296 *17*(6), 2421–2433.
- 1297 Godard, M., Joussetin, D., & Bodinier, J.-L. (2000). Relationships between geochemistry
1298 and structure beneath a palaeo-spreading centre: a study of the mantle section in the
1299 Oman ophiolite. *Earth and Planetary Science Letters*, *180*(1-2), 133–148.
- 1300 Griffiths, R. W., & Campbell, I. H. (1990). Stirring and structure in mantle starting plumes.
1301 *Earth and Planetary Science Letters*, *99*(1-2), 66–78.

- 1302 Grove, T. L., Kinzler, R. J., & Bryan, W. B. (1992). Fractionation of mid-ocean ridge basalt
1303 (MORB). *Mantle flow and melt generation at mid-ocean ridges*, 71, 281–310.
- 1304 Harvey, J., Gannoun, A., Burton, K. W., Rogers, N. W., Alard, O., & Parkinson, I. J. (2006).
1305 Ancient melt extraction from the oceanic upper mantle revealed by Re–Os isotopes in
1306 abyssal peridotites from the Mid-Atlantic ridge. *Earth and Planetary Science Letters*,
1307 244(3), 606–621.
- 1308 He, Q., Xiao, L., Balta, B., Gao, R., & Chen, J. (2010). Variety and complexity of the Late-
1309 Permian Emeishan basalts: reappraisal of plume–lithosphere interaction processes.
1310 *Lithos*, 119(1-2), 91–107.
- 1311 Heinonen, J. S., Jennings, E. S., & Riley, T. R. (2015). Crystallisation temperatures of the
1312 most Mg-rich magmas of the Karoo LIP on the basis of Al-in-olivine thermometry.
1313 *Chemical Geology*, 411, 26–35.
- 1314 Helz, R. T., & Thornber, C. R. (1987). Geothermometry of Kilauea Iki lava lake, Hawaii.
1315 *Bulletin of volcanology*, 49(5), 651–668.
- 1316 Herzberg, C. (2004). Partial crystallization of mid-ocean ridge basalts in the crust and
1317 mantle. *Journal of Petrology*, 45(12), 2389–2405.
- 1318 Herzberg, C. (2011). Basalts as temperature probes of Earth’s mantle. *Geology*, 39(12),
1319 1179–1180.
- 1320 Herzberg, C., & Asimow, P. (2015). PRIMELT3 MEGA.XLSM software for primary magma
1321 calculation: Peridotite primary magma MgO contents from the liquidus to the solidus.
1322 *Geochemistry, Geophysics, Geosystems*, 16(2), 563–578.
- 1323 Herzberg, C., & Asimow, P. D. (2008). Petrology of some oceanic island basalts:
1324 PRIMELT2. XLS software for primary magma calculation. *Geochemistry, Geophysics,*
1325 *Geosystems*, 9(9).
- 1326 Herzberg, C., Gasparik, T., & Sawamoto, H. (1990). Origin of mantle peridotite: constraints
1327 from melting experiments to 16.5 GPa. *Journal of Geophysical Research: Solid Earth*,
1328 95(B10), 15779–15803.
- 1329 Herzberg, C., & Gazel, E. (2009). Petrological evidence for secular cooling in mantle plumes.
1330 *Nature*, 458(7238), 619.
- 1331 Herzberg, C., & O’Hara, M. (2002). Plume-associated ultramafic magmas of Phanerozoic
1332 age. *Journal of Petrology*, 43(10), 1857–1883.
- 1333 Herzberg, C., Raterron, P., & Zhang, J. (2000). New experimental observations on the an-
1334 hydrous solidus for peridotite KLB-1. *Geochemistry, Geophysics, Geosystems*, 1(11).
- 1335 Hirose, K., & Kushiro, I. (1993). Partial melting of dry peridotites at high pressures:
1336 determination of compositions of melts segregated from peridotite using aggregates of
1337 diamond. *Earth and Planetary Science Letters*, 114(4), 477–489.
- 1338 Hirschmann, M. M. (2000). Mantle solidus: Experimental constraints and the effects of
1339 peridotite composition. *Geochemistry, Geophysics, Geosystems*, 1(10).
- 1340 Hirschmann, M. M., & Stolper, E. M. (1996). A possible role for garnet pyroxenite in the
1341 origin of the “garnet signature” in MORB. *Contributions to Mineralogy and Petrology*,
1342 124(2), 185–208.
- 1343 Hoggard, M. J., Parnell-Turner, R., & White, N. (2020). Hotspots and mantle plumes revis-
1344 ited: Towards reconciling the mantle heat transfer discrepancy. *Earth and Planetary*
1345 *Science Letters*, 542, 116317.
- 1346 Hole, M. J., & Millett, J. (2016). Controls of mantle potential temperature and lithospheric
1347 thickness on magmatism in the north Atlantic Igneous Province. *Journal of Petrology*,
1348 57(2), 417–436.
- 1349 Hole, M. J., & Natland, J. H. (2019). Magmatism in the North Atlantic Igneous Province;
1350 mantle temperatures, rifting and geodynamics. *Earth-Science Reviews*.
- 1351 Holland, T. J., Green, E. C., & Powell, R. (2018). Melting of peridotites through to
1352 granites: a simple thermodynamic model in the system KNCFMASHTOCr. *Journal*
1353 *of Petrology*.
- 1354 Holland, T. J., & Powell, R. (2011). An improved and extended internally consistent
1355 thermodynamic dataset for phases of petrological interest, involving a new equation
1356 of state for solids. *Journal of Metamorphic Geology*, 29(3), 333–383.

- 1357 Iwamori, H., McKenzie, D., & Takahashi, E. (1995). Melt generation by isentropic mantle
1358 upwelling. *Earth and Planetary Science Letters*, *134*(3-4), 253–266.
- 1359 Jenkins, J., Cottaar, S., White, R. S., & Deuss, A. (2016). Depressed mantle discontinuities
1360 beneath Iceland: Evidence of a garnet controlled 660 km discontinuity? *Earth and*
1361 *Planetary Science Letters*, *433*, 159–168.
- 1362 Jennings, E. S., Gibson, S. A., & Maclennan, J. (2019). Hot primary melts and mantle
1363 source for the Paraná-Etendeka flood basalt province: New constraints from Al-in-
1364 olivine thermometry. *Chemical Geology*, *529*, 119287.
- 1365 Jennings, E. S., & Holland, T. J. (2015). A simple thermodynamic model for melting of
1366 peridotite in the system NCFMASOCr. *Journal of Petrology*, *56*(5), 869–892.
- 1367 Jennings, E. S., Holland, T. J., Shorttle, O., Maclennan, J., & Gibson, S. A. (2016).
1368 The composition of melts from a heterogeneous mantle and the origin of ferropicrite:
1369 application of a thermodynamic model. *Journal of Petrology*, *57*(11-12), 2289–2310.
- 1370 Johnston, A. D. (1986). Anhydrous PT phase relations of near-primary high-alumina basalt
1371 from the South Sandwich Islands. *Contributions to Mineralogy and Petrology*, *92*(3),
1372 368–382.
- 1373 Katz, R. F., Spiegelman, M., & Langmuir, C. H. (2003). A new parameterization of hydrous
1374 mantle melting. *Geochemistry, Geophysics, Geosystems*, *4*(9).
- 1375 Kelemen, P. B., Koga, K., & Shimizu, N. (1997). Geochemistry of gabbro sills in the
1376 crust-mantle transition zone of the Oman ophiolite: Implications for the origin of the
1377 oceanic lower crust. *Earth and Planetary Science Letters*, *146*(3-4), 475–488.
- 1378 Kerr, A. C. (2005). La Isla de Gorgona, Colombia: a petrological enigma? *Lithos*, *84*(1-2),
1379 77–101.
- 1380 Kinzler, R. J., & Grove, T. L. (1992). Primary magmas of mid-ocean ridge basalts 1.
1381 experiments and methods. *Journal of Geophysical Research: Solid Earth*, *97*(B5),
1382 6885–6906.
- 1383 Klein, E. M., & Langmuir, C. H. (1987). Global correlations of ocean ridge basalt chemistry
1384 with axial depth and crustal thickness. *Journal of Geophysical Research: Solid Earth*,
1385 *92*(B8), 8089–8115.
- 1386 Kogiso, T., Hirose, K., & Takahashi, E. (1998). Melting experiments on homogeneous
1387 mixtures of peridotite and basalt: application to the genesis of ocean island basalts.
1388 *Earth and Planetary Science Letters*, *162*(1-4), 45–61.
- 1389 Kogiso, T., Hirschmann, M., & Pertermann, M. (2004). High-pressure partial melting of
1390 mafic lithologies in the mantle. *Journal of Petrology*, *45*(12), 2407–2422.
- 1391 Kogiso, T., & Hirschmann, M. M. (2006). Partial melting experiments of bimineralec eclogite
1392 and the role of recycled mafic oceanic crust in the genesis of ocean island basalts. *Earth*
1393 *and Planetary Science Letters*, *249*(3-4), 188–199.
- 1394 Kumar, P., Kind, R., Priestley, K., & Dahl-Jensen, T. (2007). Crustal structure of Iceland
1395 and Greenland from receiver function studies. *Journal of Geophysical Research: Solid*
1396 *Earth*, *112*(B3).
- 1397 Lambart, S., Baker, M. B., & Stolper, E. M. (2016). The role of pyroxenite in basalt genesis:
1398 Melt-PX, a melting parameterization for mantle pyroxenites between 0.9 and 5 GPa.
1399 *Journal of Geophysical Research: Solid Earth*, *121*(8), 5708–5735.
- 1400 Lambart, S., Laporte, D., & Schiano, P. (2009). An experimental study of pyroxenite partial
1401 melts at 1 and 1.5 GPa: Implications for the major-element composition of mid-ocean
1402 ridge basalts. *Earth and Planetary Science Letters*, *288*(1-2), 335–347.
- 1403 Lambart, S., Laporte, D., & Schiano, P. (2013). Markers of the pyroxenite contribution
1404 in the major-element compositions of oceanic basalts: Review of the experimental
1405 constraints. *Lithos*, *160*, 14–36.
- 1406 Langmuir, C. H., Klein, E. M., & Plank, T. (1992). Petrological systematics of mid-ocean
1407 ridge basalts: constraints on melt generation beneath ocean ridges. *GMS*, *71*, 183–
1408 280.
- 1409 Lassiter, J., Byerly, B., Snow, J., & Hellebrand, E. (2014). Constraints from Os-isotope
1410 variations on the origin of Lena Trough abyssal peridotites and implications for the
1411 composition and evolution of the depleted upper mantle. *Earth and Planetary Science*

- 1412 *Letters*, 403, 178–187.
- 1413 Lee, C.-T. A., Luffi, P., Plank, T., Dalton, H., & Leeman, W. P. (2009). Constraints on the
1414 depths and temperatures of basaltic magma generation on Earth and other terrestrial
1415 planets using new thermobarometers for mafic magmas. *Earth and Planetary Science*
1416 *Letters*, 279(1-2), 20–33.
- 1417 Liu, C.-Z., Snow, J. E., Hellebrand, E., Brüggmann, G., Von Der Handt, A., Büchl, A., &
1418 Hofmann, A. W. (2008). Ancient, highly heterogeneous mantle beneath Gakkel ridge,
1419 Arctic Ocean. *Nature*, 452(7185), 311.
- 1420 Maaløe, S. (2004). The PT-phase relations of an MgO-rich Hawaiian tholeiite: the com-
1421 positions of primary Hawaiian tholeiites. *Contributions to Mineralogy and Petrology*,
1422 148(2), 236–246.
- 1423 MacLennan, J. (2008). Concurrent mixing and cooling of melts under Iceland. *Journal of*
1424 *Petrology*, 49(11), 1931–1953.
- 1425 MacLennan, J., M^cKenzie, D., & Gronvöld, K. (2001). Plume-driven upwelling under central
1426 Iceland. *Earth and Planetary Science Letters*, 194(1), 67–82.
- 1427 Mallick, S., Standish, J. J., & Bizimis, M. (2015). Constraints on the mantle mineralogy of
1428 an ultra-slow ridge: hafnium isotopes in abyssal peridotites and basalts from the 9–25
1429 E Southwest Indian Ridge. *Earth and Planetary Science Letters*, 410, 42–53.
- 1430 Matthews, S., & Shorttle, O. (2020, July). *simonwmatthews/pymelt_multinest v1.0.0*. Zen-
1431 odo. Retrieved from <https://doi.org/10.5281/zenodo.3965689> doi: 10.5281/zen-
1432 odo.3965689
- 1433 Matthews, S., Shorttle, O., & MacLennan, J. (2016). The temperature of the Icelandic man-
1434 tle from olivine-spinel aluminum exchange thermometry. *Geochemistry, Geophysics,*
1435 *Geosystems*, 17(11), 4725–4752.
- 1436 Matthews, S., Shorttle, O., & Wong, K. (2020, September). *simonwmatthews/pymelt: First*
1437 *release*. Zenodo. Retrieved from <https://doi.org/10.5281/zenodo.4011814> doi:
1438 10.5281/zenodo.4011814
- 1439 Matzen, A. K., Wood, B. J., Baker, M. B., & Stolper, E. M. (2017). The roles of pyroxenite
1440 and peridotite in the mantle sources of oceanic basalts. *Nature Geoscience*, 10(7),
1441 530.
- 1442 M^cKenzie, D., & Bickle, M. (1988). The volume and composition of melt generated by
1443 extension of the lithosphere. *Journal of petrology*, 29(3), 625–679.
- 1444 M^cKenzie, D., & O’Nions, R. (1991). Partial melt distributions from inversion of rare earth
1445 element concentrations. *Journal of Petrology*, 32(5), 1021–1091.
- 1446 M^cKenzie, D., & O’Nions, R. K. (1995). The source regions of ocean island basalts. *Journal*
1447 *of petrology*, 36(1), 133–159.
- 1448 Neave, D. A., & Putirka, K. D. (2017). A new clinopyroxene-liquid barometer, and implica-
1449 tions for magma storage pressures under Icelandic rift zones. *American Mineralogist*,
1450 102(4), 777–794.
- 1451 Nisbet, E., Cheadle, M., Arndt, N., & Bickle, M. (1993). Constraining the potential
1452 temperature of the Archaean mantle: a review of the evidence from komatiites. *Lithos*,
1453 30(3-4), 291–307.
- 1454 Niu, Y., Wilson, M., Humphreys, E. R., & O’Hara, M. J. (2011). The origin of intra-plate
1455 ocean island basalts (OIB): the lid effect and its geodynamic implications. *Journal of*
1456 *Petrology*, 52(7-8), 1443–1468.
- 1457 O’Hara, M. (1968). The bearing of phase equilibria studies in synthetic and natural systems
1458 on the origin and evolution of basic and ultrabasic rocks. *Earth-Science Reviews*, 4,
1459 69–133.
- 1460 O’Hara, M. (1965). Primary magmas and the origin of basalts. *Scottish Journal of Geology*,
1461 1(1), 19–40.
- 1462 Palme, H., & O’Neill, H. (2014). *Cosmochemical estimates of mantle composition. planets,*
1463 *asteroids, comets and the solar system, volume 2 of treatise on geochemistry . edited*
1464 *by andrew m. davis*. Elsevier.
- 1465 Parnell-Turner, R., White, N., Henstock, T., Murton, B., MacLennan, J., & Jones, S. M.
1466 (2014). A continuous 55-million-year record of transient mantle plume activity beneath

- 1467 Iceland. *Nature Geoscience*, 7(12), 914.
- 1468 Paulick, H., Bach, W., Godard, M., De Hoog, J., Suhr, G., & Harvey, J. (2006). Geochem-
 1469 istry of abyssal peridotites (Mid-Atlantic Ridge, 15 20' N, odp leg 209): implications
 1470 for fluid/rock interaction in slow spreading environments. *Chemical geology*, 234(3-4),
 1471 179–210.
- 1472 Perfit, M. R., Fornari, D., Ridley, W., Kirk, P., Casey, J., Kastens, K., ... others (1996).
 1473 Recent volcanism in the Siqueiros transform fault: picritic basalts and implications
 1474 for MORB magma genesis. *Earth and Planetary Science Letters*, 141(1-4), 91–108.
- 1475 Pertermann, M., & Hirschmann, M. M. (2003). Partial melting experiments on a MORB-
 1476 like pyroxenite between 2 and 3 GPa: Constraints on the presence of pyroxenite in
 1477 basalt source regions from solidus location and melting rate. *Journal of Geophysical
 1478 Research: Solid Earth*, 108(B2).
- 1479 Phipps Morgan, J. (2001). Thermodynamics of pressure release melting of a veined plum
 1480 pudding mantle. *Geochemistry, Geophysics, Geosystems*, 2(4).
- 1481 Powell, R., Holland, T. J., & Worley, B. (1998). Calculating phase diagrams involving
 1482 solid solutions via non-linear equations, with examples using THERMOCALC. *Journal
 1483 of metamorphic Geology*, 16(4), 577–588.
- 1484 Priestley, K., & McKenzie, D. (2006). The thermal structure of the lithosphere from shear
 1485 wave velocities. *Earth and Planetary Science Letters*, 244(1-2), 285–301.
- 1486 Putirka, K. D. (1999). Melting depths and mantle heterogeneity beneath Hawaii and the
 1487 East Pacific Rise: Constraints from Na/Ti and rare earth element ratios. *Journal of
 1488 Geophysical Research: Solid Earth*, 104(B2), 2817–2829.
- 1489 Putirka, K. D. (2005). Mantle potential temperatures at Hawaii, Iceland, and the mid-ocean
 1490 ridge system, as inferred from olivine phenocrysts: Evidence for thermally driven
 1491 mantle plumes. *Geochemistry, Geophysics, Geosystems*, 6(5).
- 1492 Putirka, K. D. (2008a). Excess temperatures at ocean islands: Implications for mantle
 1493 layering and convection. *Geology*, 36(4), 283–286.
- 1494 Putirka, K. D. (2008b). Thermometers and barometers for volcanic systems. *Reviews in
 1495 mineralogy and geochemistry*, 69(1), 61–120.
- 1496 Putirka, K. D. (2016). Rates and styles of planetary cooling on Earth, Moon, Mars, and
 1497 Vesta, using new models for oxygen fugacity, ferric-ferrous ratios, olivine-liquid Fe-Mg
 1498 exchange, and mantle potential temperature. *American Mineralogist*, 101(4), 819–
 1499 840.
- 1500 Putirka, K. D., Perfit, M., Ryerson, F., & Jackson, M. G. (2007). Ambient and excess
 1501 mantle temperatures, olivine thermometry, and active vs. passive upwelling. *Chemical
 1502 Geology*, 241(3-4), 177–206.
- 1503 Putirka, K. D., Tao, Y., Hari, K., Perfit, M. R., Jackson, M. G., & Arevalo Jr, R. (2018).
 1504 The mantle source of thermal plumes: Trace and minor elements in olivine and major
 1505 oxides of primitive liquids (and why the olivine compositions don't matter). *American
 1506 Mineralogist: Journal of Earth and Planetary Materials*, 103(8), 1253–1270.
- 1507 Reid, I., & Jackson, H. (1981). Oceanic spreading rate and crustal thickness. *Marine
 1508 Geophysical Researches*, 5(2), 165–172.
- 1509 Ribe, N. M., Tackley, P. J., & Sanan, P. (2020). The strength of the iceland plume: A
 1510 geodynamical scaling approach. *Earth and Planetary Science Letters*, 551, 116570.
- 1511 Richards, M. A., Duncan, R. A., & Courtillot, V. E. (1989). Flood basalts and hot-spot
 1512 tracks: plume heads and tails. *Science*, 246(4926), 103–107.
- 1513 Roeder, P., & Emslie, R. (1970). Olivine-liquid equilibrium. *Contributions to mineralogy
 1514 and petrology*, 29(4), 275–289.
- 1515 Rudge, J. F., MacLennan, J., & Stracke, A. (2013). The geochemical consequences of mixing
 1516 melts from a heterogeneous mantle. *Geochimica et Cosmochimica Acta*, 114, 112–143.
- 1517 Saal, A., Hart, S., Shimizu, N., Hauri, E., & Layne, G. (1998). Pb isotopic variability in melt
 1518 inclusions from oceanic island basalts, Polynesia. *Science*, 282(5393), 1481–1484.
- 1519 Salters, V. J., Mallick, S., Hart, S. R., Langmuir, C. E., & Stracke, A. (2011). Domains of
 1520 depleted mantle: New evidence from hafnium and neodymium isotopes. *Geochemistry,
 1521 Geophysics, Geosystems*, 12(8).

- 1522 Salters, V. J., & Zindler, A. (1995). Extreme $^{176}\text{Hf}/^{177}\text{Hf}$ in the sub-oceanic mantle. *Earth*
1523 *and Planetary Science Letters*, *129*(1-4), 13–30.
- 1524 Seyler, M., Lorand, J.-P., Toplis, M. J., & Godard, G. (2004). Asthenospheric metasomatism
1525 beneath the mid-ocean ridge: Evidence from depleted abyssal peridotites. *Geology*,
1526 *32*(4), 301–304.
- 1527 Shorttle, O. (2015). Geochemical variability in MORB controlled by concurrent mixing and
1528 crystallisation. *Earth and Planetary Science Letters*, *424*, 1–14.
- 1529 Shorttle, O. (2017). Geodynamics: Hot mantle rising. *Nature Geoscience*, *10*(6), 400–400.
- 1530 Shorttle, O., & MacLennan, J. (2011). Compositional trends of Icelandic basalts: Implica-
1531 tions for short-length scale lithological heterogeneity in mantle plumes. *Geochemistry*,
1532 *Geophysics, Geosystems*, *12*(11).
- 1533 Shorttle, O., MacLennan, J., & Lambart, S. (2014). Quantifying lithological variability in
1534 the mantle. *Earth and Planetary Science Letters*, *395*, 24–40.
- 1535 Shorttle, O., Matthews, S., & MacLennan, J. (2020). Finding harzburgite in the mantle.
1536 a comment on brown et al.(2020):” markov chain monte carlo inversion of mantle
1537 temperature and source composition, with application to reykjanes peninsula, ice-
1538 land” [earth planet. sci. lett. 532 (2020) 116007]. *Earth and Planetary Science Letters*,
1539 *548*, 116503.
- 1540 Shorttle, O., Rudge, J. F., MacLennan, J., & Rubin, K. H. (2016). A statistical description
1541 of concurrent mixing and crystallization during MORB differentiation: implications
1542 for trace element enrichment. *Journal of Petrology*, *57*(11-12), 2127–2162.
- 1543 Sides, I., Edmonds, M., MacLennan, J., Houghton, B. F., Swanson, D., & Steele-MacInnis,
1544 M. J. (2014b). Magma mixing and high fountaining during the 1959 Kilauea iki
1545 eruption, hawai’i. *Earth and Planetary Science Letters*, *400*, 102–112.
- 1546 Sides, I., Edmonds, M., MacLennan, J., Swanson, D., & Houghton, B. (2014a). Eruption style
1547 at Kilauea volcano in Hawai’i linked to primary melt composition. *Nature Geoscience*,
1548 *7*(6), 464.
- 1549 Smith, P. M., & Asimow, P. D. (2005). Adiaabat_1ph: A new public front-end to the MELTS,
1550 pMELTS, and pHMELTS models. *Geochemistry, Geophysics, Geosystems*, *6*(2).
- 1551 Sobolev, A., & Shimizu, N. (1994). The origin of typical NMORB: the evidence from a melt
1552 inclusion study. *Mineral. Mag. A*, *58*, 862–863.
- 1553 Sobolev, A. V., Asafov, E. V., Gurenko, A. A., Arndt, N. T., Batanova, V. G., Portnyagin,
1554 M. V., ... Krasheninnikov, S. P. (2016). Komatiites reveal a hydrous Archaean
1555 deep-mantle reservoir. *Nature*, *531*(7596), 628.
- 1556 Sobolev, A. V., Hofmann, A. W., Sobolev, S. V., & Nikogosian, I. K. (2005). An olivine-free
1557 mantle source of Hawaiian shield basalts. *Nature*, *434*(7033), 590.
- 1558 Spandler, C., & O’Neill, H. S. C. (2010). Diffusion and partition coefficients of minor and
1559 trace elements in San Carlos olivine at 1,300°C with some geochemical implications.
1560 *Contributions to Mineralogy and Petrology*, *159*(6), 791–818.
- 1561 Spice, H. E., Fitton, J. G., & Kirstein, L. A. (2016). Temperature fluctuation of the Iceland
1562 mantle plume through time. *Geochemistry, Geophysics, Geosystems*, *17*(2), 243–254.
- 1563 Stracke, A., Genske, F., Berndt, J., & Koornneef, J. M. (2019). Ubiquitous ultra-depleted
1564 domains in Earth’s mantle. *Nature Geoscience*, *12*(10), 851–855.
- 1565 Stracke, A., Snow, J. E., Hellebrand, E., Von Der Handt, A., Bourdon, B., Birbaum, K., &
1566 Günther, D. (2011). Abyssal peridotite Hf isotopes identify extreme mantle depletion.
1567 *Earth and Planetary Science Letters*, *308*(3), 359–368.
- 1568 Takahashi, E., Nakajima, K., & Wright, T. L. (1998). Origin of the Columbia River basalts:
1569 melting model of a heterogeneous plume head. *Earth and Planetary Science Letters*,
1570 *162*(1-4), 63–80.
- 1571 Takahashi, E. (1986). Melting of a dry peridotite KLB-1 up to 14 GPa: Implications on
1572 the origin of peridotitic upper mantle. *Journal of Geophysical Research: Solid Earth*,
1573 *91*(B9), 9367–9382.
- 1574 Takahashi, E., & Scarfe, C. M. (1985). Melting of peridotite to 14 GPa and the genesis of
1575 komatiite. *Nature*, *315*(6020), 566–568.
- 1576 Takahashi, E., Shimazaki, T., Tsuzaki, Y., & Yoshida, H. (1993). Melting study of a

- 1577 peridotite KLB-1 to 6.5 GPa, and the origin of basaltic magmas. *Philosophical Trans-*
 1578 *actions of the Royal Society of London. Series A: Physical and Engineering Sciences,*
 1579 *342*(1663), 105–120.
- 1580 Tao, Y., Putirka, K. D., Hu, R.-Z., & Li, C. (2015). The magma plumbing system of the
 1581 Emeishan large igneous province and its role in basaltic magma differentiation in a
 1582 continental setting. *American Mineralogist*, *100*(11-12), 2509–2517.
- 1583 Thompson, R., & Gibson, S. (2000). Transient high temperatures in mantle plume heads
 1584 inferred from magnesian olivines in Phanerozoic picrites. *Nature*, *407*(6803), 502.
- 1585 Thompson, R., Gibson, S., Dickin, A., & Smith, P. (2001). Early Cretaceous basalt and
 1586 picrite dykes of the southern Etendeka region, NW Namibia: windows into the role
 1587 of the Tristan mantle plume in Paraná–Etendeka magmatism. *Journal of Petrology*,
 1588 *42*(11), 2049–2081.
- 1589 Thomson, A., & Maclennan, J. (2012). The distribution of olivine compositions in Icelandic
 1590 basalts and picrites. *Journal of Petrology*, *54*(4), 745–768.
- 1591 Toplis, M. (2005). The thermodynamics of iron and magnesium partitioning between
 1592 olivine and liquid: criteria for assessing and predicting equilibrium in natural and
 1593 experimental systems. *Contributions to Mineralogy and Petrology*, *149*(1), 22–39.
- 1594 Trela, J., Gazel, E., Sobolev, A. V., Moore, L., Bizimis, M., Jicha, B., & Batanova, V. G.
 1595 (2017). The hottest lavas of the Phanerozoic and the survival of deep Archaean reser-
 1596 voirs. *Nature Geoscience*, *10*(6), 451.
- 1597 Trela, J., Vidito, C., Gazel, E., Herzberg, C., Class, C., Whalen, W., . . . Alvarado, G. E.
 1598 (2015). Recycled crust in the Galápagos plume source at 70 Ma: Implications for
 1599 plume evolution. *Earth and Planetary Science Letters*, *425*, 268–277.
- 1600 Trønnes, R. G., & Frost, D. J. (2002). Peridotite melting and mineral–melt partitioning
 1601 of major and minor elements at 22–24.5 GPa. *Earth and Planetary Science Letters*,
 1602 *197*(1-2), 117–131.
- 1603 Tsuruta, K., & Takahashi, E. (1998). Melting study of an alkali basalt JB-1 up to 12.5
 1604 GPa: behavior of potassium in the deep mantle. *Physics of the Earth and Planetary*
 1605 *Interiors*, *107*(1-3), 119–130.
- 1606 Turcotte, D., & Schubert, G. (2014). *Geodynamics*. Cambridge University Press.
- 1607 Wagner, T., & Grove, T. (1998). Melt/harzburgite reaction in the petrogenesis of tholeiitic
 1608 magma from Kilauea volcano, Hawaii. *Contributions to Mineralogy and Petrology*,
 1609 *131*(1), 1–12.
- 1610 Walter, M. J. (1998). Melting of garnet peridotite and the origin of komatiite and depleted
 1611 lithosphere. *Journal of Petrology*, *39*(1), 29–60.
- 1612 Wan, Z., Coogan, L. A., & Canil, D. (2008). Experimental calibration of aluminum par-
 1613 titioning between olivine and spinel as a geothermometer. *American Mineralogist*,
 1614 *93*(7), 1142–1147.
- 1615 Wang, Z., & Gaetani, G. A. (2008). Partitioning of Ni between olivine and siliceous eclog-
 1616 ite partial melt: experimental constraints on the mantle source of Hawaiian basalts.
 1617 *Contributions to Mineralogy and Petrology*, *156*(5), 661–678.
- 1618 Warren, J. (2016). Global variations in abyssal peridotite compositions. *Lithos*, *248*,
 1619 193–219.
- 1620 Warren, J., Shimizu, N., Sakaguchi, C., Dick, H., & Nakamura, E. (2009). An assessment of
 1621 upper mantle heterogeneity based on abyssal peridotite isotopic compositions. *Journal*
 1622 *of Geophysical Research: Solid Earth*, *114*(B12).
- 1623 Warren, J., & Shirey, S. (2012). Lead and osmium isotopic constraints on the oceanic
 1624 mantle from single abyssal peridotite sulfides. *Earth and Planetary Science Letters*,
 1625 *359*, 279–293.
- 1626 Waterton, P., Pearson, D. G., Kjarsgaard, B., Hulbert, L., Locock, A., Parman, S., & Davis,
 1627 B. (2017). Age, origin, and thermal evolution of the ultra-fresh 1.9 Ga Winnipegosis
 1628 Komatiites, Manitoba, Canada. *Lithos*, *268*, 114–130.
- 1629 Watson, S. (1993). Rare earth element inversions and percolation models for Hawaii. *Journal*
 1630 *of Petrology*, *34*(4), 763–783.

- 1631 Watson, S., & M^cKenzie, D. (1991). Melt generation by plumes: a study of Hawaiian
1632 volcanism. *Journal of Petrology*, *32*(3), 501–537.
- 1633 Watts, A., & Ten Brink, U. (1989). Crustal structure, flexure, and subsidence history of
1634 the Hawaiian islands. *Journal of Geophysical Research: Solid Earth*, *94*(B8), 10473–
1635 10500.
- 1636 Wessel, P. (2016). Regional–residual separation of bathymetry and revised estimates of
1637 Hawaii plume flux. *Geophysical Journal International*, *204*(2), 932–947.
- 1638 White, R. S. (1993). Melt production rates in mantle plumes. *Philosophical Transactions of
1639 the Royal Society of London. Series A: Physical and Engineering Sciences*, *342*(1663),
1640 137–153.
- 1641 White, R. S. (1997). Mantle plume origin for the Karoo and Ventersdorp flood basalts,
1642 South Africa. *South African Journal of Geology*, *100*(4), 271–282.
- 1643 White, R. S., & M^cKenzie, D. (1989). Magmatism at rift zones: the generation of volcanic
1644 continental margins and flood basalts. *Journal of Geophysical Research: Solid Earth*,
1645 *94*(B6), 7685–7729.
- 1646 White, R. S., & M^cKenzie, D. (1995). Mantle plumes and flood basalts. *Journal of
1647 Geophysical Research: Solid Earth*, *100*(B9), 17543–17585.
- 1648 White, R. S., M^cKenzie, D., & O’Nions, R. K. (1992). Oceanic crustal thickness from seismic
1649 measurements and rare earth element inversions. *Journal of Geophysical Research:
1650 Solid Earth*, *97*(B13), 19683–19715.
- 1651 Wieser, P. E., Edmonds, M., Maclennan, J., Jenner, F. E., & Kunz, B. E. (2019). Crystal
1652 scavenging from mush piles recorded by melt inclusions. *Nature Communications*,
1653 *10*(1), 1–11.
- 1654 Willhite, L. N., Jackson, M. G., Blichert-Toft, J., Bindeman, I., Kurz, M. D., Halldórsson,
1655 S. A., ... Byerly, B. L. (2019). Hot and heterogenous high-³He/⁴He components:
1656 New constraints from proto-Iceland plume lavas from Baffin island. *Geochemistry,
1657 Geophysics, Geosystems*.
- 1658 Wilson, J. T. (1973). Mantle plumes and plate motions. *Tectonophysics*, *19*(2), 149–164.
- 1659 Workman, R. K., & Hart, S. R. (2005). Major and trace element composition of the depleted
1660 MORB mantle (DMM). *Earth and Planetary Science Letters*, *231*(1), 53–72.
- 1661 Xu, R., & Liu, Y. (2016). Al-in-olivine thermometry evidence for the mantle plume origin
1662 of the Emeishan large igneous province. *Lithos*, *266*, 362–366.
- 1663 Xu, Y., Chung, S.-L., Jahn, B.-m., & Wu, G. (2001). Petrologic and geochemical constraints
1664 on the petrogenesis of Permian–Triassic Emeishan flood basalts in southwestern China.
1665 *Lithos*, *58*(3-4), 145–168.
- 1666 Yasuda, A., Fujii, T., & Kurita, K. (1994). Melting phase relations of an anhydrous mid-
1667 ocean ridge basalt from 3 to 20 GPa: Implications for the behavior of subducted
1668 oceanic crust in the mantle. *Journal of Geophysical Research: Solid Earth*, *99*(B5),
1669 9401–9414.
- 1670 Zhang, J., & Herzberg, C. (1994). Melting experiments on anhydrous peridotite KLB-1 from
1671 5.0 to 22.5 GPa. *Journal of Geophysical Research: Solid Earth*, *99*(B9), 17729–17742.
- 1672 Zhukova, I., O’Neill, H., & Campbell, I. H. (2017). A subsidiary fast-diffusing substitution
1673 mechanism of Al in forsterite investigated using diffusion experiments under controlled
1674 thermodynamic conditions. *Contributions to Mineralogy and Petrology*, *172*(7), 53.